RECEIVED
FEB 24 1994
OSTI

IS-T 1641

Probability of Detection Models for Eddy Current NDE Methods

by

Rajesh, S. N.

MS Thesis submitted to Iowa State University

Ames Laboratory, U.S. DOE
Iowa State University
Ames, Iowa 50011

Date Transmitted: April 30, 1993

PREPARED FOR THE U.S. DEPARTMENT OF ENERGY
UNDER CONTRACT NO. W-7405-Eng-82.

MASTER

DISCLAIMER

Printed in the United States of America

Available from
National Technical Information Service
U.S. Department of Commerce
5265 Port Royal Road
Springfield, VA 22161

TABLE OF CONTENTS

ACKNOWLEDGMENTS

I would like to express my deepest gratitude and appreciation to Dr. Lalita Udpa for the guidance and support given to me throughout the course of this research. She was very understanding and her professional and personal encouragement will leave a lasting impression. I also thank her for the patience and the number of hours she put into proof reading this manuscript suggesting several important changes which are responsible for its present form.

I would like to thank Dr. Satish Udpa for serving on my graduate committee. I am indebted to Dr. Udpa for his constant encouragement, technical advise and invaluable assistance throughout this project which gave me added zeal for this research.

I would also like to thank Dr. William Lord and Dr. Richard Groeneveld for consenting to serve on my graduate committee.

This work was supported by the FAA - Center for Aviation Systems Reliability, operated by the Ames Laboratory, USDOE, for the Federal Aviation Administration under contract No. W-7405-ENG-82 with Iowa State University. Grateful acknowledgment is made for their support.

ABSTRACT

A considerable amount of attention has been focused in recent years towards the development of probability of detection (POD) models for a variety of nondestructive evaluation (NDE) methods. Interest in these models is motivated by a desire to quantify the variability introduced during the process of testing. As an example, sources of variability involved in eddy current methods of NDE include those caused by variations in liftoff, material properties, probe canting angle, scan format, surface roughness and measurement noise. Numerical models have been extensively used to model physical processes underlying NDE phenomena. Such models have been used, for example, to predict the transducer response for a given specimen geometry, defect configuration and test conditions. These models, however, are deterministic in nature and do not take into account variabilities associated with the inspection carried out in the field. This has limited the utility of deterministic models to practitioners in general since a considerable difference can exist between the nominal value of the transducer response predicted by the model and the actual measurement.

This thesis presents a comprehensive POD model for eddy current NDE. Eddy current methods of nondestructive testing are used widely in industry to inspect a variety of nonferromagnetic and ferromagnetic materials. The development of a comprehensive POD model is therefore of significant importance. The model incorporates several sources of variability characterized by a multivariate Gaussian distribution and employs finite element analysis to predict the signal distribution. The method of mixtures is then used for estimating optimal threshold values. The research demonstrates the use of a finite element model within a probabilistic framework to predict the spread in the measured signal for eddy current nondestructive methods.

Using the signal distributions for various flaw sizes the POD curves for varying defect parameters have been computed. In contrast to experimental POD models, the cost of generating such curves is very low and complex defect shapes can be handled very easily. The results are also operator independent.

CHAPTER 1. INTRODUCTION

1.1. Problem Definition

Nondestructive evaluation (NDE) is the inspection and evaluation of materials, parts, and other products without the adverse impairment of their properties and serviceability. NDE is widely used to detect and characterize flaws in engineering structures such as airplane wheels and frames, bridges, nuclear reactor pressure vessels and so on. Such defects could result in failure during service and have disastrous consequences. Generally most defects are in the form of cracks which occur due to cyclic loads and environmental attack or during manufacture either in welds or castings.

A variety of nondestructive testing (NDT) techniques such as ultrasonics, X-rays and electromagnetic methods have evolved to cater to various applications. A generic nondestructive test system consists of an energy source which interacts with the specimen under inspection. The response of this interaction constitutes an NDT signal. For instance, examples of electromagnetic NDE methods are potential drop, magnetic flux leakage field and eddy current methods. One of the most commonly used electromagnetic methods is the eddy current method of nondestructive testing. Eddy current methods of nondestructive testing are widely used in various industries for detection and characterization of flaws in conducting, ferromagnetic and non ferromagnetic materials. These methods are based on the changes occurring in the coil impedance when a coil excited by an alternating current source is brought close to a conducting material.

In order to use a nondestructive test method effectively, it is necessary to understand fully the forward problem describing the field/flaw interaction. Hence there is a need for theoretical models that represent the influence of various test and defect parameters on the measured transducer signal. The modeling involves the solution of the partial differential equation underlying the physical phenomenon. Analytical, numerical and hybrid methods are available for solving the governing equations. Analytical approaches to the modeling of electromagnetic field and defect interaction have been unsuccessful due to the awkward boundaries associated with the three dimensional defect shapes and the need for simplifying assumptions to obtain the solutions. The inadequacy of analytical methods together with the arrival of relatively high speed computational power have led to the increased popularity of numerical techniques such as the finite difference and finite element methods. These methods are flexible and capable of taking into account awkward defect geometries and nonlinearities in material properties. Finite element modeling for characterizing NDE phenomena was pioneered by Lord [13,14,15] and has been used successfully in several applications. However these models are deterministic in nature and do not take into account the variabilities associated with the measurement process.

In any nondestructive testing system the process of NDE signal measurement is not deterministic and signals generated by identical flaws or alternatively signals obtained by repeated scans of the same flaw are seldom the same. As an example, if 1000 scans are made in an eddy current testing setup, we will seldom get the same signal every time due to a number of variabilities acting on the system. For instance, in some eddy current testing situations, the variability introduced in the measurement can be caused by several factors such as liftoff, surface roughness, material properties such as conductivity and permeability, scan format and so on. The process is therefore not deterministic and has a stochastic component associated with it.

In order to design a practical NDE system the cost, safety and performance requirements of the system which depends on the testing conditions have to be determined. Also the detection capability of various NDE techniques, in detecting a critical flaw of certain size and shape is required. These issues are generally quantified by means of parameters such as probability of detection (POD), probability of false alarm (PFA) and probability of false acceptance (POFA).

The three major approaches for estimating the probability of detection of a flaw are classified as experimental, model based and hybrid. The experimental POD estimates rely on the use of a large number of inspectors testing a large number of flawed specimens. However the determination of probability of detection of defects requires an extensive set of measurements to obtain statistically sound estimates. Hence this approach is time consuming and expensive particularly since it involves the machining of difficult defect shapes in a large number of samples and involves a large number of operators. The model based POD approach involves simulating on a digital computer the measurements one would make in an experimental set up. The flaw signal and the effect of the variabilities are predicted by the computer model. These models serve as a test bed for generating defect signatures that are expensive to replicate experimentally. The hybrid model uses a combination of the first two approaches. The theoretical predictions help in determining flaw signals and a certain amount of experimental data is used to account for the noise parameter.

The model based approach, used in this research, constitutes a powerful tool for addressing a wide variety of issues relating to NDE reliability. These estimates can for example not only provide insight into factors affecting detectability and hence the performance of an NDT system but also assist in determining optimum test parameters. These estimates are very useful in assessing the applicability of a particular technique given a testing situation. Model based POD estimators can also play a crucial role as a vehicle for interpolating and extrapolating results obtained from experimental POD models. Such use can lead to significant cost benefits particularly in situations involving defects that are difficult and expensive to replicate in a laboratory in large numbers.

1.2. Scope of Thesis

This thesis investigates the feasibility of a probability of detection model for eddy current inspection techniques. The finite element measurement model is perturbed by factors influencing the measurement to generate the ensemble of signals characterized by conditional probability density functions. The probability of detection, probability of false alarm and probability of false acceptance are then estimated by appropriate integrations of the density functions.

Chapter 2 introduces the different types of nondestructive testing techniques currently in practice and then focuses on the principles of eddy current testing technique. Chapter 3 discusses the numerical modeling of the eddy current NDT phenomena. The two dimensional (2D) axisymmetric numerical modeling of the electromagnetic phenomena used in the measurement model to predict the measurement signals is explained. Details involving the calculation of eddy current probe impedance using the direct method and the energy method are provided.

Chapter 4 discusses the probability of detection models for NDE techniques with emphasis on the eddy current method. A description of existing techniques for POD calculations and details involved in the model based POD estimation are explained. Chapter 5 presents the simulation results followed by discussions and comments of the 2D axisymmetric POD model.

Chapter 6 presents some concluding remarks and identifies areas for future research activity. The need for a full three dimensional POD model for simulating some of the test variabilities and the challenges involved in the development of the 3D POD model are discussed. Techniques for addressing these challenges are also presented and finally a comprehensive list of references is included.

CHAPTER 2. PRINCIPLES OF NONDESTRUCTIVE TESTING

2.1. Introduction

Nondestructive testing methods depend on some form of energy source as the probing source which interacts with the specimen under inspection as shown in Figure 2.1. The response of the field/flaw interaction is picked up by the receiving transducer to produce an output signal. The output signal is processed and passed through an inversion block the output of which gives

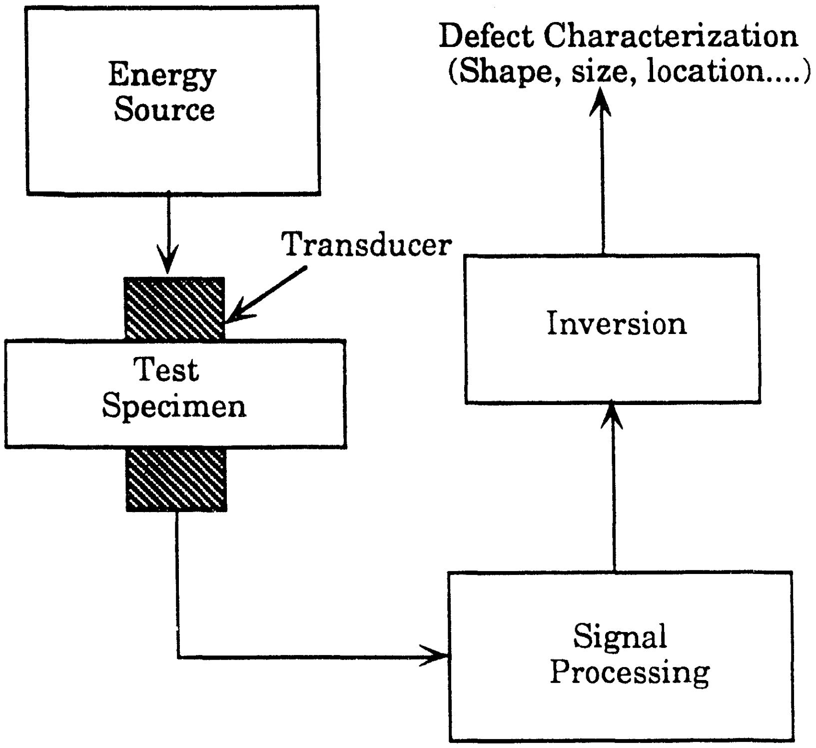

Figure 2.1: Components of an NDT system [4]

the defect characterization information such as the shape, location and dimensions of the flaw.

2.2. Methods of Nondestructive Testing

A variety of methods of nondestructive testing are in existence and these rely on different forms of energy as the probing source. Some examples of NDT techniques include visual methods, dye penetrant, magnetic, ultrasonic, radiographic, electromagnetic and so on. Some of the most commonly used nondestructive testing methods are the ultrasonic, radiography and electromagnetic methods, and these techniques are described briefly below.

2.2.1. Ultrasonic NDT

The ultrasonic method is probably one of the oldest methods of NDT. This method makes use of sound waves as the probing source to detect cracks in a test specimen. The principles of ultrasonic inspection are illustrated in Figure 2.2. As shown in the figure the pulser converts electrical energy int sound energy. The audible frequency [1] is in the range of about 10 to 20000 Hz and sound waves above this range are called 'ultrasound'. A couplant such as glycerine or oil of medium viscosity is required to couple the ultrasonic waves into the material. The ultrasonic waves travel through the material under test with some attenuation and are reflected whenever a discontinuity is encountered in the material. As seen in the figure the signal contains reflections due to front wall, the flaw and the back wall.

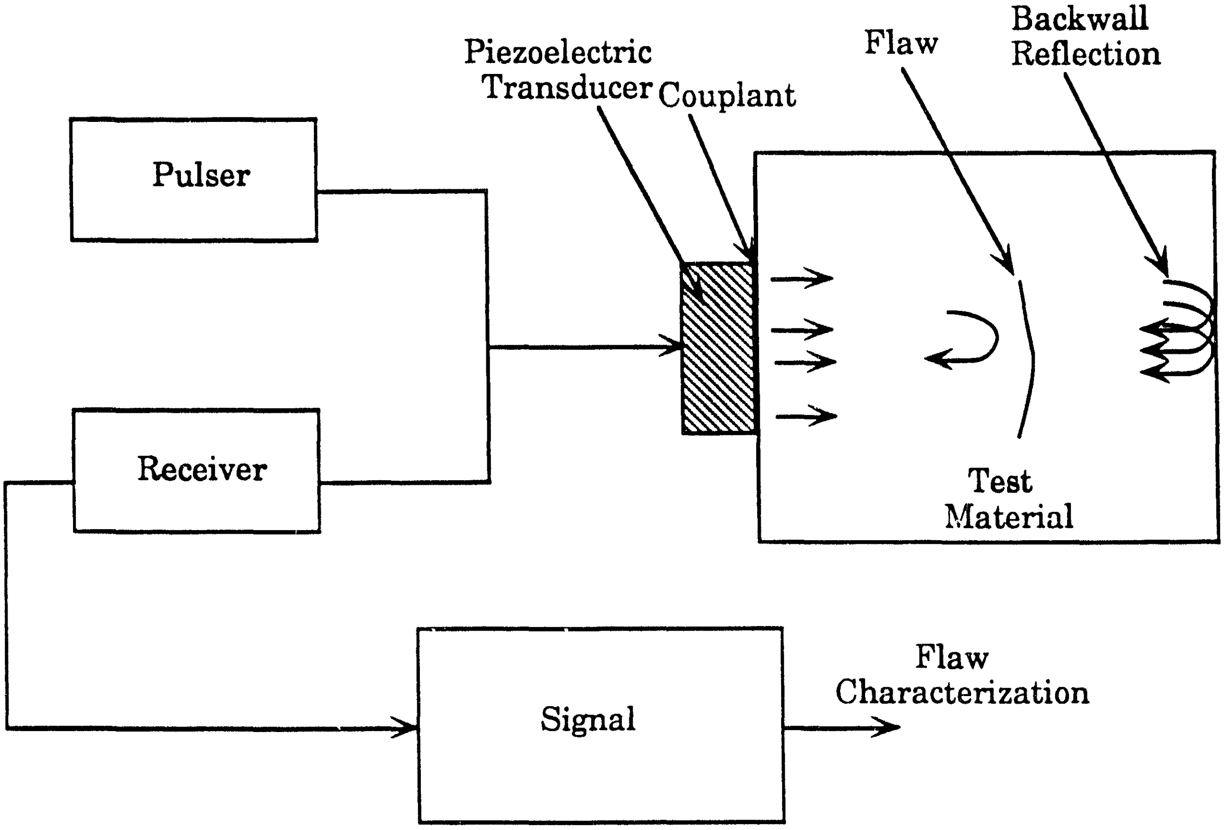

Figure 2.2: Principles of ultrasonic inspection

Figure 2.3 shows a typical signal from the ultrasonic testing, as a function of time, for a single position of the transducer. The paramcters of interest indicating the presence and location of the flaw are the amplitude of the reflected signal and the time elapsed between the incident and the reflected signals, referred to as the time of flight. The amplitude of the signal provides information about the flaw size and the time of flight is a measure of the distance of the flaw from the surface of the material. This signal is picked up by the transducer and processed in order to determine the characteristics of

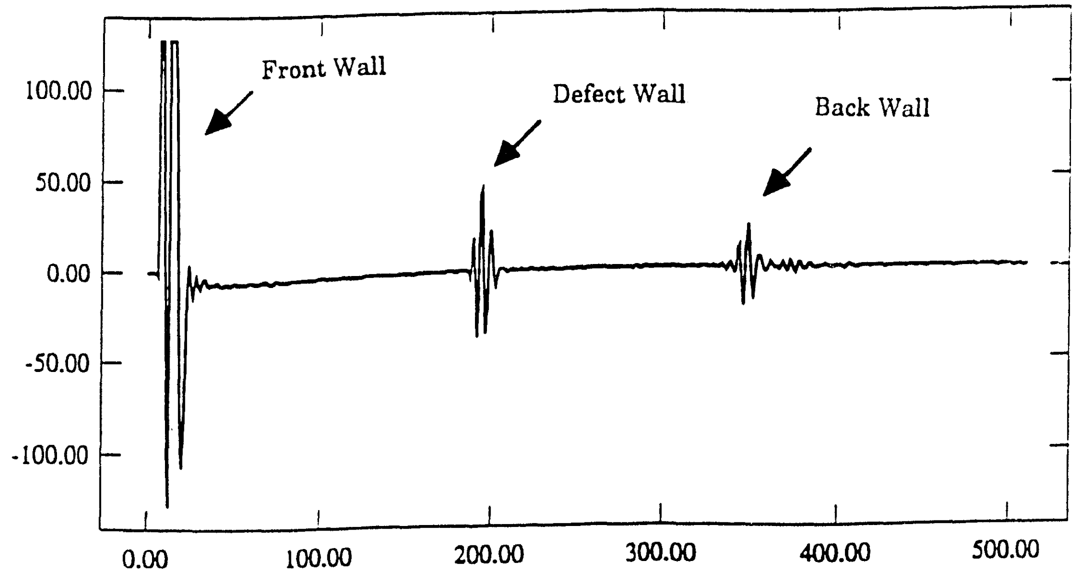

Figure 2.3: A typical ultrasonic NDT A-scan signal

the material.

There are basically three modes of operation defined as the A-scan, B-scan and C-scan carrying different types of information. As shown in Figure 2.3, for a single position of the transducer we get a one dimensional recording of the echoes of the incident signal, as a function of time, indicating the presence of a flaw at a certain depth. This is the A-scan mode. The B-scan mode involves a set of A-scans taken with a transducer scanning along the length of the material. This gives a cross-sectional view of the flaw distribution. The C-scan mode consists of a set of B-scans, where in the probe scans the material in a regular raster and the defects are represented by bright patches. Here a two dimensional display of the test surface in a plan view is obtained.

2.2.2. Radiographic NDT

Radiographic NDT involves the use of x-rays or gamma rays as the interrogating energy source. Both gamma rays and X-rays are electromagnetic radiations of high frequencies with wavelengths ranging from 10^{-7} to 10^{-11} cms. Gamma rays are generated by transition of a radioactive nuclei from a high energy state to a more stable lower energy state. X-rays are produced when a beam of high energy (high velocity) electrons strikes a target material wherein the kinetic energy of the electrons is converted to electromagnetic radiation. Due to the high energy content these radiations have a high penetrating power and hence can penetrate most materials. Figure 2.4 shows a typical set-up for radiographic NDT. The intensity of the beam of energy transmitted through the material is reduced with the thickness traversed by the beam and can be expressed as

$$I_t = I_0 \exp(- \mu t) \tag{2.1}$$

where t is the thickness of the material, I_0 and I_t are the incident and transmitted energies respectively and μ the linear absorption coefficient dependent on the material properties. The transmitted energy is recorded on a photographic film. The photographic film is then analyzed to determine the characteristics of the material. A variety of parameters such as the type of film, size and shape of the beam source, exposure time, source to film distance, energy of the beam and developing material have to be carefully chosen in order to get good results.

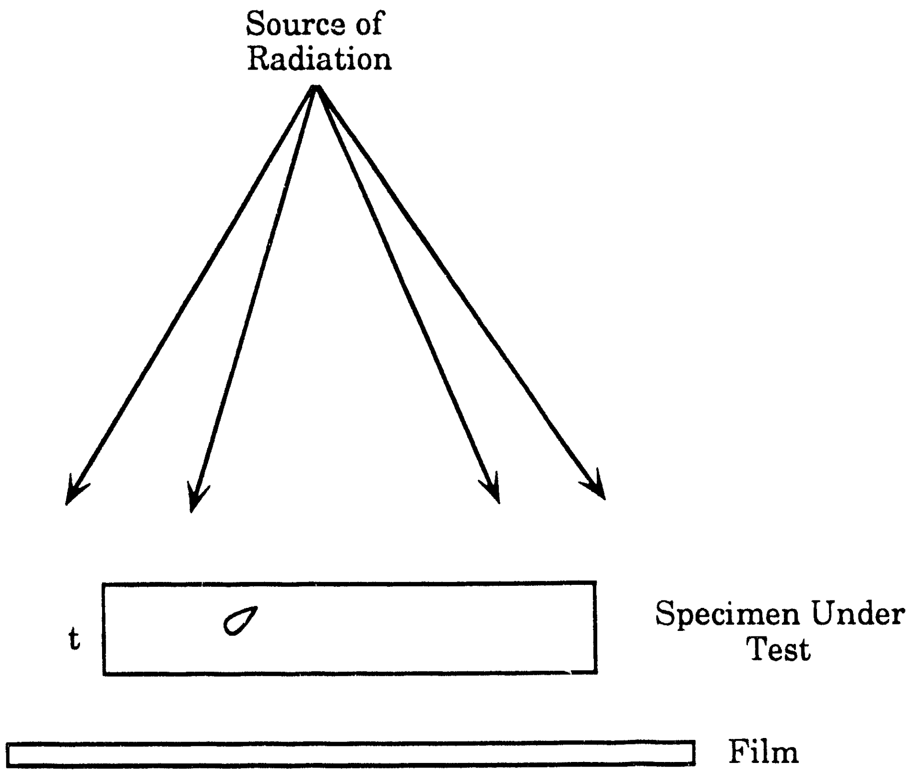

Figure 2.4: Test set up in radiographic NDT [4]

2.2.3. Electromagnetic NDT

Electromagnetic methods of nondestructive testing methods are based on principles of electric and magnetic fields. Examples of electromagnetic NDE methods are potential drop, magnetostatic leakage field and eddy current testing methods. The leakage field method, used in inspecting ferromagnetic materials, uses a direct current (static) as the excitation source. The eddy current method involves excitation of a coil by a low frequency (quasi-static) alternating current.

The magnetic field is varied due to a variation in one or more of the electrical properties of the test object such as magnetic permeability, electric permittivity or electric conductivity. The magnetic field is monitored by measuring the induced current or voltage or both in the exciting coils. The most commonly used electromagnetic test is the eddy current nondestructive test. The principles involved in this technique are explained in the following sections.

2.3. Principles of Eddy Current Testing

The eddy current nondestructive testing is based on the phenomena of electromagnetic induction. The principles of this technique are illustrated in Figure 2.5. When a coil is excited by an alternating current, in accordance with the Maxwell-Ampere law, a time varying magnetic field (primary field) is set up given by equation

$$\int_C \mathbf{H.dl} = \int \int_S \mathbf{J.ds} \tag{2.2}$$

where displacement currents are neglected.

When the coil is brought close to a conducting material, due to the Maxwell-Faraday law, the primary field associated with the coil induces an emf in the material given by the equation

$$\int_C \mathbf{E.dl} = - \int \int_S \dot{\mathbf{B}}\mathbf{.ds} \tag{2.3}$$

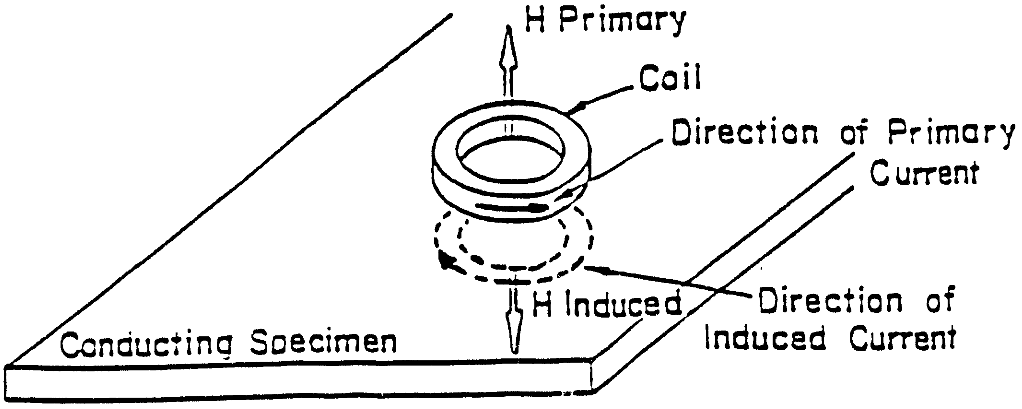

Figure 2.5: Physical principles of the eddy current method [3]

which in turn induces eddy currents that flow in closed paths. According to Lenz's law the EMF and induced currents are directed so as to oppose the change which produces them. The magnetic field set up by the induced eddy currents (secondary fields) opposes the primary magnetic field associated with the coil. When the test specimen is nonferromagnetic the net flux linkages of the coil decreases which in turn decreases the inductance of the coil. Accompanying the decrease in the inductance is an increase in resistance of the coil since the eddy current losses incurred in the specimen has to be met by the source of primary excitation.

The underlying process is more complicated when the test specimen is ferromagnetic. Along with the decrease in inductance due to the influence of eddy currents is an increase in inductance due to the higher permeability of the material. The latter effect is more predominant and hence when the coil is brought close to a ferromagnetic specimen the over all inductance of the coil increases along with an increase in its resistance.

A defect present in the test material would change the flow of eddy currents, as shown in Figure 2.6, and hence cause a change in the coil impedance. The defect interrupts the flow of eddy currents and hence a crack

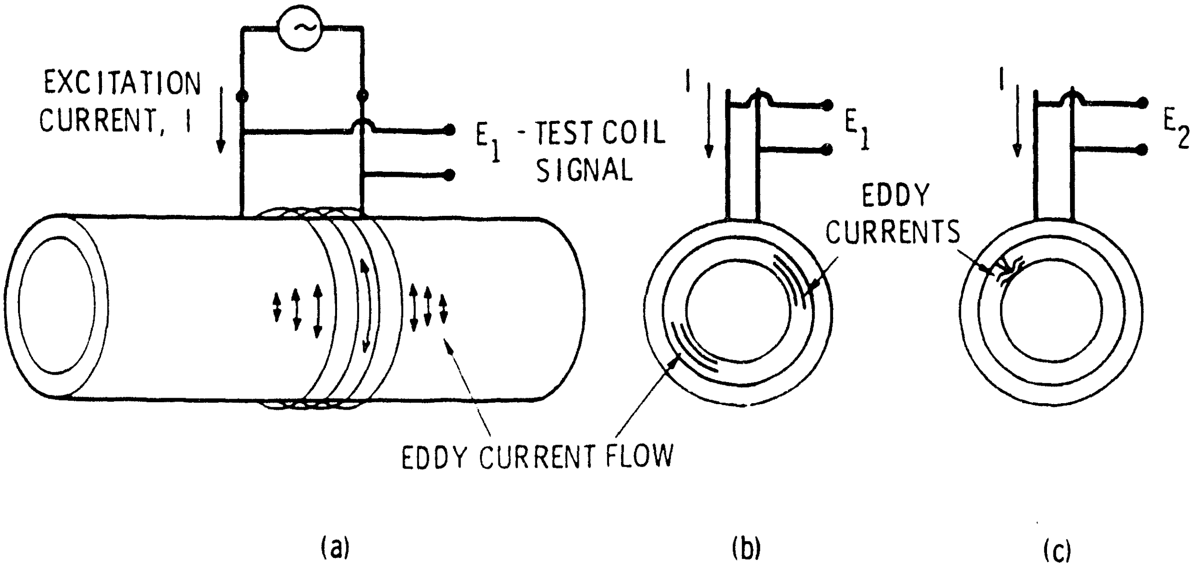

Figure 2.6: Tubing test using a single encircling coil : a) side view; b) and c) are cross-sectional views of current distribution for tubing without and with a longitudinal flaw respectively [2]

with its plane perpendicular to the current flow would produce a larger signal than if its plane is parallel to the eddy currents. As an example a very thin axisymmetric flaw in the direction of the eddy currents would have a very small effect on the current flow resulting in a small output signal.

The change in the coil impedance produced by a flaw in general is very small when compared to the no flaw impedance of the coil. In addition the signal includes effects of various factors such as material conductivity, permeability, liftoff, surface roughness, frequency, scan format, temperature and so on. These factors can mask the changes due to defects making the detection of the defect very difficult. The effect, of these factors and their variations on the signal has been investigated in this thesis and these effects are quantified by estimating probability of detection of a given flaw.

2.4. The Eddy Current Phenomenon

The governing equation for eddy current phenomena can be derived from Maxwell's equations. In differential form [3,4] the Maxwell's equations can be written as

$$\nabla \times \mathbf{E} = -\frac{\partial \mathbf{B}}{\partial t} \tag{2.4}$$

$$\nabla \times \mathbf{H} = \mathbf{J} + \frac{\partial \mathbf{D}}{\partial t} \tag{2.5}$$

$$\nabla . \mathbf{B} = 0 \tag{2.6}$$

$$\nabla . \mathbf{D} = \rho \tag{2.7}$$

and the constitutive relations for isotropic, linear and homogeneous medium are

$$\mathbf{B} = \mu \mathbf{H} \tag{2.8}$$

$$\mathbf{D} = \varepsilon \mathbf{E} \tag{2.9}$$

$$\mathbf{J} = \sigma \mathbf{E} \tag{2.10}$$

where

ε is the electric permittivity (farads/m)

μ is the magnetic permeability (Henry/m)

σ is the electric conductivity (mhos/m).

Since div **B** = 0, **B** can be expressed as the curl of the vector magnetic potential **A** given by

$$\mathbf{B} = \nabla \times \mathbf{A} \tag{2.11}$$

Substituting for **B** in equation (2.4)

$$\nabla \times \mathbf{E} = -\nabla \times \frac{\partial \mathbf{A}}{\partial t} \tag{2.12}$$

$$\text{or} \quad \nabla \times \left(\mathbf{E} + \frac{\partial \mathbf{A}}{\partial t} \right) = 0 \tag{2.13}$$

Using the vector identities we express

$$\mathbf{E} + \frac{\partial \mathbf{A}}{\partial t} = -\nabla \phi \tag{2.14}$$

where ϕ is the scalar electric potential.

Substituting (2.10) in equation (2.14) we have

$$\mathbf{J} = -\left(\sigma \frac{\partial \mathbf{A}}{\partial t} + \sigma \nabla \phi \right) \tag{2.15}$$

$$= -\sigma \frac{\partial \mathbf{A}}{\partial t} + \mathbf{J_s} \tag{2.16}$$

where $\mathbf{J_S} = -\sigma \nabla \phi$ is the source current density and $\mathbf{J_e} = \sigma \frac{\partial \mathbf{A}}{\partial t}$ is the induced eddy current density

At the excitation frequencies for eddy current testing the displacement current $\frac{\partial \mathbf{D}}{\partial t}$ in equation (2.5) is negligibly small in comparison with the conduction current density $\mathbf{J}$ and equation (2.5) reduces to

$$\nabla \times \mathbf{H} = \mathbf{J} \tag{2.17}$$

Substituting equations (2.8) and (2.16) into (2.17)

$$\left(\nabla \times \frac{\mathbf{B}}{\mu} \right) = \mathbf{J_s} - \sigma \frac{\partial \mathbf{A}}{\partial t} \tag{2.18}$$

Using (2.11)

$$\left(\nabla x \frac{1}{\mu}(\nabla x A)\right) = \mathbf{J_s} - \sigma\frac{\partial A}{\partial t} \tag{2.19}$$

Assuming a homogeneous medium and using the vector identity

$$\nabla x\, (\nabla x A) = \nabla(\nabla . A) - \nabla^2 A \tag{2.20}$$

we arrive at equation (2.21)

$$\frac{1}{\mu}\nabla^2 A = \sigma\frac{\partial A}{\partial t} - J_s \tag{2.21}$$

where $\nabla.\mathbf{A} = 0$ choosing the Coulomb gauge.

Assuming that the fields vary harmonically in steady state we can express **A** as

$$A = A_o e^{-j\omega t} \tag{2.22}$$

where ω is the angular frequency.

Substituting (2.22) into (2.21), we obtain

$$\frac{1}{\mu}\nabla^2 A = j\omega\sigma A - J_s \tag{2.23}$$

The exact solution of equation (2.23) can be obtained analytically only for very simple geometries such as infinite half plane media. In most realistic test situations complex geometries and awkward boundary conditions make the solution of equation (2.23) very difficult and numerical methods such as the finite element or the finite difference techniques are often used to solve the equation.

2.5. Skin Effect

The magnetic field, during eddy current testing, decays exponentially with the depth of the material. Hence the eddy current methods of nondestructive testing are generally not very effective in detecting subsurface flaws far away from the surface of the material. The depth at which the amplitude of the magnetic field falls to 1/e times the field at the surface is called the skin depth. The value of the skin depth can be determined from Maxwell's equations as follows:

Using equation (2.10) equation (2.17) can be written as

$$\nabla \mathrm{x} \mathbf{H} = \sigma \mathbf{E} \tag{2.24}$$

Taking the curl on both sides

$$\nabla \mathrm{x}(\nabla \mathrm{x} \mathbf{H}) = \nabla \mathrm{x}(\sigma \mathbf{E}) \tag{2.25}$$

Using the vector identities in equation (2.20)

$$-\nabla^2\mathbf{H} + \nabla(\nabla.\mathbf{H}) = \nabla x(\sigma\mathbf{E}) \tag{2.26}$$

From equation (2.6) $\nabla.\mathbf{B} = 0$, implies $\nabla.\mathbf{H} = 0$ and hence

$$\nabla^2\mathbf{H} = -\nabla x(\sigma\mathbf{E}) \tag{2.27}$$

From equations (2.4) and (2.8) we have

$$\nabla x\mathbf{E} = -\frac{\partial\mathbf{B}}{\partial t} = -\mu\frac{\partial\mathbf{H}}{\partial t} \tag{2.28}$$

Substituting (2.28) in (2.27) we have

$$\nabla^2\mathbf{H} = \mu\sigma\frac{\partial\mathbf{H}}{\partial t} \tag{2.29}$$

Assuming the field varies harmonically in the steady state with time **H** can be expressed as

$$\mathbf{H} = \mathbf{H}_0\, e^{j\omega t} \tag{2.30}$$

where ω is the angular frequency.

Substituting (2.30) in (2.29) we have

$$\nabla^2 \mathbf{H} = (j\omega\mu\sigma)\,\mathbf{H} \tag{2.31}$$

$$= r^2\,\mathbf{H} \tag{2.32}$$

where $$r^2 = j\omega\mu\sigma \tag{2.33}$$

For an infinite sheet of current in the Y direction on the YZ plane the magnetic field intensity is in the Z direction with no components in the X or Y directions. Also there are no variations in H with y or z due to the plane wave conditions. Equation (2.31) reduces to

$$\frac{\partial^2 \mathbf{H_z}}{\partial \mathbf{x}^2} = r^2\,\mathbf{H_z} \tag{2.34}$$

and the solution to equation (2.34) is given by

$$\mathbf{H_z} = \mathbf{H_o}\, e^{-rx} \tag{2.35}$$

where r defined by equation (2.33), called the propagation constant, is given by

$$r = (j\omega\mu\sigma)^{1/2} \tag{2.36}$$

$$= \left(\frac{\omega\mu\sigma}{2}\right)^{1/2} + j\left(\frac{\omega\mu\sigma}{2}\right)^{1/2} \tag{2.37}$$

Hence equation (2.36) can be written as

$$\mathbf{H_z} = \mathbf{H_o}\, e^{-x/\delta} \,.\, e^{-jx/\delta} \tag{2.38}$$

where

$$\delta = \left(\frac{\omega\mu\sigma}{2}\right)^{-1/2} = \left(\frac{1}{\pi f\mu\sigma}\right)^{1/2} \tag{2.39}$$

is called the skin depth.

It can be seen from equation (2.35) that at the depth $x = \delta$

$$\mathbf{H_z} = \left(\frac{1}{e}\right)\mathbf{H_o} \tag{2.40}$$

The skin depth is a function of the excitation frequency as well as the permeability and conductivity of the material. For detecting subsurface flaws generally the frequency of excitation is low as this would result in a greater skin depth.

CHAPTER 3. NUMERICAL MODELING OF EDDY CURRENT NDT PHENOMENA

3.1. Introduction

In order to use a nondestructive test method effectively, it is essential to understand fully the forward problem describing the field/flaw interaction. Hence there is a need for a theoretical model that represents the influence of various test and defect parameters on the measured transducer signal. Theoretical measurement models also serve as a test bed for generating defect signatures that are expensive to replicate experimentally. The modeling involves the solution of the partial differential equation governing the underlying physical phenomena. Figure 3.1 shows the schematic representation of the measurement model which takes the excitation source as the input and gives the predicted signal at the output by solving the underlying physical process. Analytical, numerical and hybrid methods have been in existence for solving the governing equations.

Although analytical techniques offer closed form solutions, they suffer from the drawback that these solutions make several simplifying assumptions relating to the test geometry. The inadequacy of analytical methods, together with the arrival of relatively inexpensive high speed computational power have led to the increased popularity of numerical techniques such as the finite difference and finite element methods. These methods are flexible and are capable of taking into account awkward defect geometries and nonlinearities

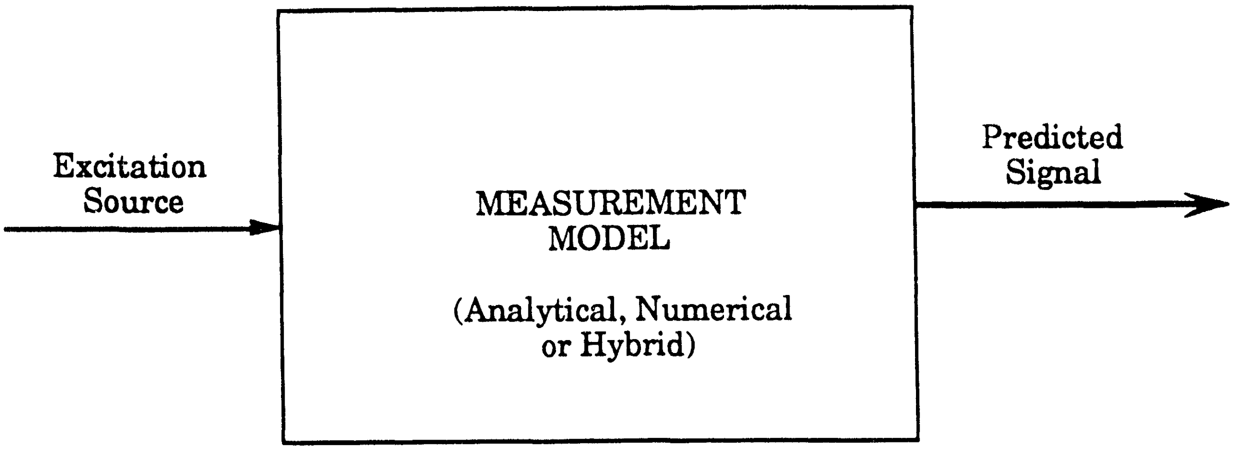

Figure 3.1: A typical NDT system

in material properties. Numerical methods that are widely in use in electromagnetic NDT are the finite difference and the finite element methods. This thesis uses the measurement model based on finite element analysis which is explained in more detail in the following sections.

3.2. The Finite Element Method

Finite element analysis has been widely used in various fields including structural analysis, mechanics, heat transfer for solving a variety of problems. The range of applications spread to a wide variety of areas after Zienkiewicz and others [5-6] showed that the method could be applied to the solution of any differential equation. The finite element method was first applied to problems in electrical engineering by Silvester and Chari [7] who used the method to solve the differential equations governing the electromagnetic field problems in electrical machines. The solutions to the fields and flux in turbogenerators has been examined by Chari [8] and Demerdash [9]. The finite element analysis has been applied by Chari [10] for studying the eddy current problems in magnetic structures. Anderson [11] used this technique to study the transformer leakage fields and Brauer [12] for studying the induced magnetic fields and currents in transformers.

The method was popularized in the area of electromagnetic NDT by Lord. Lord and Hwang [13,14] first used the finite element analysis for modeling active magnetic leakage fields around defects in ferromagnetic specimens. Lord and Yen [15] and Udpa [16] then developed a two-dimensional model for studying the residual leakage fields. These models are based on the governing elliptic differential equations for magnetostatic phenomena. Lord and Palanisamy [17-19] developed a two dimensional axisymmetric finite element model to study the variable reluctance probe and later extended the model to describe quasistatic eddy current phenomena described by parabolic differential equation. A three dimensional finite element model for eddy current and magnetostatic NDT problems was later developed by Lord and Ida [20,21]. Finite element model for hyperbolic equations describing wave phenomena have been developed by Lord and Ludwig for ultrasonic NDT.

The finite element method is based on the principles of variational calculus and is documented in several texts [22]. The solution to the governing differential equation involves the incorporation of the equation in an integral form using an energy functional. The energy functional, which represents the energy of the system whose stationary value is a minimum, is minimized resulting in the solution to the governing equation.

Once the energy functional for the system is determined the finite element formulation consists of the following steps.

1. The region of interest is discretized with a suitable mesh consisting of a number of elements connected at the common nodal points as shown in Figure 3.2.

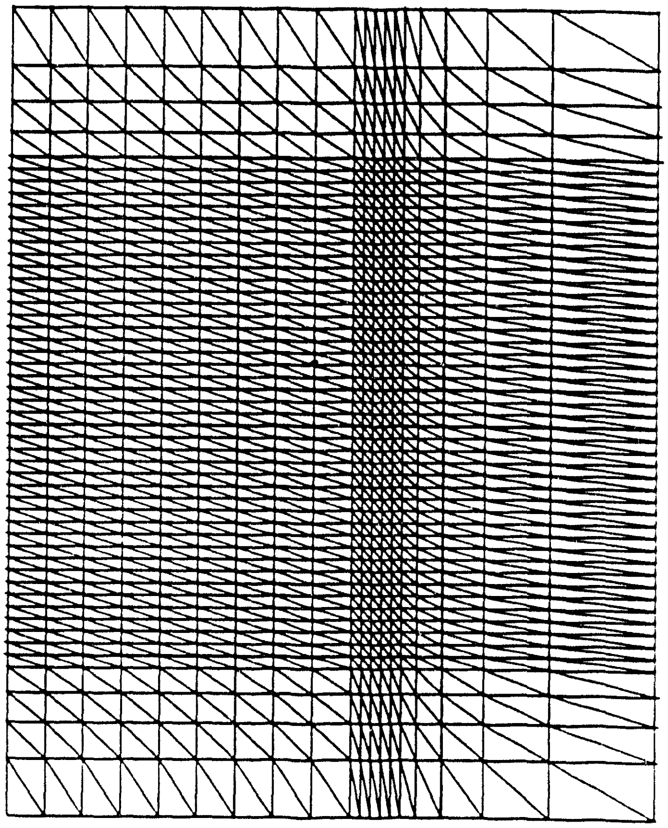

Figure 3.2: A typical finite element mesh

2. The nodes and the elements of the different materials in the regions are identified and numbered.

3. An interpolating function, which approximates the continuous field over each element in terms of the nodal point values is defined in such a way that the field is continuous across the element boundaries. The interpolating function can be linear or nonlinear and depends on the variations of the field in the test geometry.

4. Minimization of the energy functional with respect to the unknown nodal point values results in a matrix equation.

5. The solution of the matrix equation yields the field values in the region of interest.

These steps are discussed in greater detail, in the axisymmetric finite element formulation, next.

3.3. Axisymmetric Finite Element Formulation of the Eddy Current Phenomena

The finite element formulations for the 2D axisymmetric eddy current phenomena was developed by Lord and Palanisamy [17-19]. Since this model is used in this thesis, the formulation is given here for the sake of completeness. The equation governing the eddy current phenomena is the diffusion equation derived in chapter 2 and is given by

$$\frac{1}{\mu}\nabla^2 A = j\omega\sigma A - \mathbf{J_s} \tag{3.1}$$

For axisymmetric geometries equation (3.1) reduces to the 2D form

$$\frac{1}{\mu}\left(\frac{\partial^2 A}{\partial r^2} + \frac{1}{r}\frac{\partial A}{\partial r} + \frac{\partial^2 A}{\partial z^2} - \frac{A}{r^2}\right) = j\omega\sigma A - J_s \qquad (3.2)$$

The corresponding energy functional obtained from the variational principles is

$$F = \int\int_R \left(\frac{1}{2\mu}\left[\left|\frac{\partial A}{\partial r} + \frac{A}{r}\right|^2 + \left|\frac{\partial A}{\partial z}\right|^2 \right] + \frac{j\omega\sigma}{2}|A|^2 - J_s \,.\, A \right) r\,dr\,dz \qquad (3.3)$$

where the energies corresponding to the magnetic field, eddy currents and the source current are represented by the first second and third terms inside the integrand respectively.

Figure 3.3 shows a two dimensional triangular element where A_i, A_j, and A_k are the nodal point field values. A linear interpolating function for the

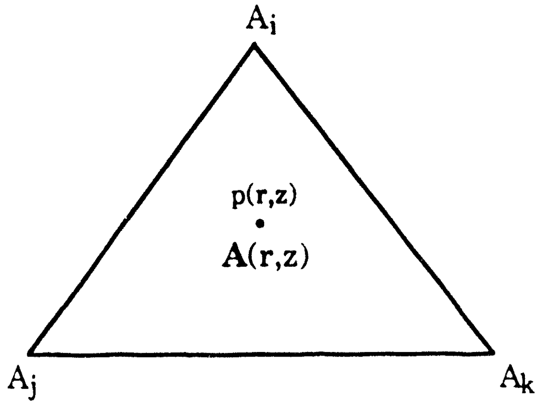

Figure 3.3: A triangular element of the finite element mesh

vector magnetic field at any point (r,z) is given by

$$A(r,z) = \alpha_1 + \alpha_2 r + \alpha_3 z \tag{3.4}$$

Substituting the nodal point values in (3.4) gives

$$\begin{aligned} A_i &= \alpha_1 + \alpha_2 r_i + \alpha_3 z_i \\ A_j &= \alpha_1 + \alpha_2 r_j + \alpha_3 z_j \\ A_k &= \alpha_1 + \alpha_2 r_k + \alpha_3 z_k \end{aligned} \tag{3.5}$$

where (r_i,z_i), (r_j,z_j) and (r_k,z_k) are the coordinates of the nodes i, j and k respectively.

Putting equations (3.5) in a matrix form we get equation (3.6)

$$\begin{bmatrix} A_i \\ A_j \\ A_k \end{bmatrix} = \begin{bmatrix} 1 & r_i & z_i \\ 1 & r_j & z_j \\ 1 & r_k & z_k \end{bmatrix} \begin{bmatrix} \alpha_1 \\ \alpha_2 \\ \alpha_3 \end{bmatrix} \tag{3.6}$$

For each element e we can write

$$[\alpha]_e = [G]_e \, [A]_e \tag{3.7}$$

where

$$[\alpha]_e = \begin{bmatrix} \alpha_1 \\ \alpha_2 \\ \alpha_3 \end{bmatrix} \tag{3.8}$$

$$[A]_e = \begin{bmatrix} A_i \\ A_j \\ A_k \end{bmatrix} \tag{3.9}$$

$$[G]_e = \begin{bmatrix} 1 & r_i & z_i \\ 1 & r_j & z_j \\ 1 & r_k & z_k \end{bmatrix}^{-1} \tag{3.10}$$

$$= \frac{1}{2\Delta} \begin{bmatrix} (r_j z_k - r_k z_j) & (r_k z_i - r_i z_k) & (r_i z_j - r_j z_i) \\ (z_j - z_k) & (z_k - z_i) & (z_i - z_j) \\ (r_k - r_j) & (r_i - r_k) & (r_j - r_i) \end{bmatrix} = \frac{1}{2\Delta} \begin{bmatrix} a_i & a_j & a_k \\ b_i & b_j & b_k \\ c_i & c_j & c_k \end{bmatrix} \tag{3.11}$$

Where Δ is the area of the triangular element given by

$$\begin{vmatrix} 1 & r_i & z_i \\ 1 & r_j & z_j \\ 1 & r_k & z_k \end{vmatrix} = 2\Delta \tag{3.12}$$

Substituting equation (3.7) in equation (3.4) for each element e with i, j, and k as the nodes we get

$$\mathbf{A}(r,z) = [\,1 \quad r \quad z\,]\,[G]_e\,[A]_e \tag{3.13}$$

Substituting equations (3.9) and (3.11) and simplifying we can rewrite equation (3.13) as

$$\mathbf{A}(r,z) = N_i A_i + N_j A_j + N_k A_k \tag{3.14}$$

Where

$$N_i = \frac{1}{2a}[\,(r_j z_k - r_k z_j) + (z_j - z_k)\,r + (r_k - r_j)\,z]$$

$$N_j = \frac{1}{2a}[\,(r_k z_i - r_i z_k) + (z_k - z_i)\,r + (r_i - r_k)\,z] \qquad (3.15)$$

$$N_k = \frac{1}{2a}[\,(r_i z_j - r_j z_i) + (z_i - z_j)\,r + (r_j - r_i)\,z]$$

N_i, N_j and N_k are called the shape functions which can be linear or nonlinear in nature. These functions relate the field at any point within the element to the fields at the nodes. Nonlinear interpolating functions are described at length in [23]. This thesis however confines to application of linear interpolating functions. Approximation of the magnetic vector potential values , **A**, over the entire domain is accomplished by covering the solution region **A**(r,z) by a set of interconnected triangular elements over which a linear variation of **A** is assumed. The continuity of the solution surface is assured as the field along the edge shared by two neighboring elements is specified uniquely by the values of the fields at the nodes shared by the two elements.

The solution to the governing equation is obtained by minimizing the energy functional given in equation (3.3), which is done on an element by element basis. For each element, with nodes i, j, and k, the partial derivative of the energy functional, F_e, with respect to the nodal point values of the field, is equated to zero given by

$$\frac{\partial F_e}{\partial \mathbf{A}_l} = 0 \qquad l = 1,2,3 \qquad (3.16)$$

where the partial derivative, for each of the elements, is given by

$$\frac{\partial F_e}{\partial \mathbf{A}_l} = \int \int_R \Big(\frac{1}{\mu}\Big[\Big(\frac{\partial \mathbf{A}}{\partial r} + \frac{\mathbf{A}}{r}\Big)\Big(\frac{\partial}{\partial \mathbf{A}_l}\Big(\frac{\partial \mathbf{A}}{\partial r}\Big) + \frac{\partial}{\partial \mathbf{A}_l}\Big(\frac{\mathbf{A}}{r}\Big)\Big) + \frac{\partial \mathbf{A}}{\partial z}.\frac{\partial}{\partial \mathbf{A}_l}\Big(\frac{\partial \mathbf{A}}{\partial z}\Big)\Big]$$

$$+ j\omega\sigma A\frac{\partial \mathbf{A}}{\partial \mathbf{A}_l} - \mathbf{J}_s.\frac{\partial \mathbf{A}}{\partial \mathbf{A}_l}\Big)\, r\, dr dz\ ,\ l = 1,2,3 \qquad (3.17)$$

Substituting for the values of the magnetic vector potential value within the element given by equation (3.14) into (3.17) results in a mathematical equation of the form

$$[\,[S]_e + j\,[R]_e\,]\ \ [A]_e = [Q]_e \qquad (3.18)$$

for each element where $[S]_e$ is a 3 x 3 matrix given by

$$[S]_e = \frac{r_c}{4a\,\mu}\begin{bmatrix} (b_i' b_i' + c_i\, c_i) & (b_i' b_j' + c_j\, c_j) & (b_i' b_k' + c_i\, c_k) \\ (b_j' b_i' + c_j\, c_i) & (b_j' b_j' + c_j\, c_j) & (b_j' b_k' + c_j\, c_k) \\ (b_k' b_i' + c_k\, c_i) & (b_k' b_j' + c_k\, c_j) & (b_k' b_k' + c_k\, c_k) \end{bmatrix} \qquad (3.19)$$

where

$b_k' = b_k + \frac{2\,a}{3r_c}$, k = i, j,k and r_c is the centroid of the element.

$[R]_e$ is a 3 x 3 element matrix given by

$$[R]_e = \frac{\omega\sigma a r_c}{12}\begin{bmatrix} 2 & 1 & 1 \\ 1 & 2 & 1 \\ 1 & 1 & 2 \end{bmatrix} \qquad (3.20)$$

$[Q]_e$ is a 3 x 1 element matrix formed from the complex current source density, $\mathbf{J_s}$, given by

$$[Q]_e = \frac{\mathbf{J_s}\, ar_c}{3}\begin{bmatrix} 1 \\ 1 \\ 1 \end{bmatrix} \tag{3.21}$$

The unknown variables are the vector potential values at the nodes of the element given by

$$[A]_e = \begin{bmatrix} \mathbf{A_i} \\ \mathbf{A_j} \\ \mathbf{A_k} \end{bmatrix} \tag{3.22}$$

Equations of the form shown in (3.18) for each of the elements are assembled together in a global matrix equation. Following the method of assembly described in [24-26] we have

$$[\mathbf{K}][\mathbf{A}] = [\mathbf{Q}] \tag{3.23}$$

where $[\mathbf{K}]$ is called the N x N stiffness matrix

$[\mathbf{Q}]$ and $[\mathbf{A}]$ are N dimensional vectors with

$$[\mathbf{A}] = [\mathbf{A_1}, \mathbf{A_2} \ldots\ldots. \mathbf{A_N}]^T \tag{3.24}$$

If the material is assumed to be linear and isotropic the stiffness matrix is banded, symmetric and sparse and hence allows storage of the matrix in a compact form.

The boundary conditions are incorporated using the ' blasting technique'. This technique involves multiplication of the diagonal element in the stiffness matrix corresponding to a boundary node by a large number and the corresponding element in the [Q] vector replaced by the boundary value multiplied by the large number. This will ensure that the off diagonal terms in that row are neglected as they are very small when compared to the diagonal element and hence the boundary node is tied down to the boundary value specified.

The global matrix is solved, after incorporating appropriate boundary conditions, material properties and the current density in each element, for the magnetic vector potentials at each of the nodes. Various quantities of interest such as the flux density, eddy current density, probe coil impedance etc. that can be calculated from the magnetic vector potential values are described in [27,28].

3.4. Calculation of the Eddy Current Probe Impedance

Once the magnetic vector potential values at all the nodes in the mesh region are determined, the probe impedance which is our parameter of interest can be computed. Two different approaches commonly used to estimate this value, are the direct and energy methods and are described in more detail next.

3.4.1. Direct Method

The impedance of a single turn coil (probe) of radius r carrying an alternating current of I_s amperes is given by

$$Z = \frac{V}{I_s} \tag{3.25}$$

where **V** is the RMS phasor voltage induced in the coil, expressed in terms of the electric field intensity **E** as

$$V = -\int_c E \cdot dl \tag{3.26}$$

From equation (2.13) we have

$$\mathbf{E} = -\frac{\partial A}{\partial t} - \nabla \phi \tag{3.27}$$

Assuming that the field varies harmonically with frequency ω given by the equation

$$A = \mathbf{A}_o e^{-j\omega t} \tag{3.28}$$

we have

$$\mathbf{E} = -j\omega\mathbf{A} - \nabla \phi \tag{3.29}$$

Since the induced voltage is independent of the gradient of the scalar potential $\nabla\phi$, substituting (3.29) into (3.26) we have

$$V = j\omega \int_c A \, . \, dl \tag{3.30}$$

From (3.25) the impedance of the coil is given by

$$Z = \frac{j\omega}{I_s} \int_c A \, . \, dl \tag{3.31}$$

which for a single turn coil of radius r is

$$Z = j \, \frac{2\pi\omega \, rA}{I_s} \tag{3.32}$$

the real and imaginary part of which can be interpreted as the resistive and reactive components of the impedance.

The coil impedance however is calculated in an approximate manner using the finite element method. Consider the cross-section of the coil, discretized by triangular elements. If the dimensions of the elements are small then the vector magnetic potential of all the turns covered by the element i can be approximated by the centroidal value A_{ci} and similarly the radius of all the turns in the element can be approximated by the centroidal value r_{ci}. From equation (3.32) the impedance for each turn within the element i is given by

$$Z_i = j\frac{2\pi\omega\, r_{ci}\, A_{ci}}{I_s} \tag{3.33}$$

If N_s is the total number of turns in the coil cross-section, N_t turns/m^2, the turn density of the element, and a_i the area of the element given by equation (3.12) the total impedance of all the turns in the element i is given by

$$Z_i = j\frac{2\pi\omega\, r_{ci}\, A_{ci}\, a_i\, N_t}{I_s} \tag{3.34}$$

If the number of elements in the cross-section of the coil is N_c then the total impedance is given by

$$Z_i = j\frac{2\pi\omega\, N_t}{I_s}\sum_{i=1}^{N_c} a_i\, r_{ci}\, A_{ci} \tag{3.35}$$

The coil impedance in a 2D or axisymmetric problem can be computed using the method explained here. This method assumes that the magnetic vector potential values are constant along the source (2D) or in the circumferential direction of the coil (axisymmetric). However this is not true in the case of 3D problems. An alternate method to compute the impedance based on the calculation of the stored and dissipated energies is explained in the following section.

3.4.2. Energy Method

The impedance of a coil can be calculated from the energy of the system [29, 30] since the inductance and the resistance are associated with the stored and dissipated energies, in the system, respectively. The stored energy W in the system can be given by

$$\text{Stored energy } W = \frac{1}{2}\int_v \mathbf{B.H}\, dv \tag{3.30}$$

From equation (3.30) assuming constant reluctivity in each direction the energy stored in a finite element of volume V_i can be written, in terms of the components of B alone, as

$$W_i = \frac{1}{2}(v_x B_x^2 + v_y B_y^2 + v_z B_z^2)\, V_i \tag{3.31}$$

where v_x, v_y and v_z are the reluctivities in the corresponding directions.

From the relation between the magnetic flux density and vector magnetic potential B we have:

$$\begin{aligned} B_x &= \frac{\partial A_z}{\partial y} - \frac{\partial A_y}{\partial z} \\ B_y &= \frac{\partial A_x}{\partial z} - \frac{\partial A_z}{\partial x} \\ B_z &= \frac{\partial A_y}{\partial x} - \frac{\partial A_x}{\partial y} \end{aligned} \tag{3.32}$$

Substituting this in equation (3.31) and summing over all the elements (N) in the mesh region, the total stored energy in the system is given by

$$W = \sum_{i=1}^{N} \left[\nu_x \left(\frac{\partial A_{zi}}{\partial yi} - \frac{\partial A_{yi}}{\partial zi} \right)^2 + \nu_y \left(\frac{\partial A_{xi}}{\partial zi} - \frac{\partial A_{zi}}{\partial xi} \right)^2 + \nu_z \left(\frac{\partial A_{yi}}{\partial xi} - \frac{\partial A_{xi}}{\partial yi} \right)^2 \right] V_i \quad (3.33)$$

The inductance of the coil can then be calculated be calculated using

$W = 0.5\ L\ I_s^2$ which gives

$$L = 2W/I_s^2 \quad (3.34)$$

where I_s is the current in the source coil.

The resistance of the coil is associated with the dissipated energy in the system. The dissipated energy in a finite element of volume V_i is given by

$$P_i = \frac{V_i\,|J_{ei}|^2}{\sigma} \quad (3.35)$$

where J_{ei} is the eddy current density and was derived earlier as

$$J_{ei} = -j\,\omega\sigma A_{ci} \quad (3.36)$$

where A_{ci} is the centroidal magnetic vector potential value for the element i. Substituting equation (3.36) in (3.35) and summing over all the elements in the mesh region, the total dissipated energy is given by

$$P = \sum_{i=1}^{N} P_i = \sum_{i=1}^{N} V_i \sigma \omega^2 |A_{ci}|^2 \tag{3.37}$$

Using $P = I^2 R$ the resistance of the coil is given by

$$R = P/I_s^2 \tag{3.38}$$

and the coil impedance by

$$Z = R + j\omega L \tag{3.39}$$

The above method is equally applicable to two dimensional and axisymmetric problems and is explained in detail in [29, 30].

The above formulation does not take the total number of turns (N_s) into consideration. By definition the total flux linkages in a coil with N_s turns is equal to $N_s\phi$ where ϕ is the flux linkages due to a coil with 1 turn. Multiplying the corresponding values of the magnetic flux density and the vector potential value by N in equations (3.31) and (3.36) we arrive at the impedance of the coil with N_s turns to be

$$Z_N = N_s^2 Z \tag{3.40}$$

where Z is the impedance of the coil with 1 turn.

3.4.3. Comparison of the Direct Method with the Energy Method

Although the energy approach is a necessity for 3D applications, the approach has several limitations when compared to the direct method:

1. The energy calculations use squared values of the magnetic vector potential. Consequently the original information regarding phase with respect to the source is lost.
2. The calculation of the stored energy involves the space differentiation of the magnetic vector potential which is done with very little extra effort in the finite element model. However this introduces severe errors, when the discretization of the region is coarse as is the case in 3D calculations.
3. The energy calculation involves summing over the entire mesh region and hence the resulting impedance reflects the source as a whole. It is not possible to calculate the impedance of the individual coils in a differential eddy current probe. A solution to this difficulty, in the case of linear problems, is discussed in [29].

3.5. Calculation of the Flux Density and the Eddy Current Density

Once the vector magnetic potentials (A) are computed, the formulation of the flux and eddy current densities for the axisymmetric two dimensional case has been dealt with in [3].

The flux density (B) can be calculated using the relation

$$\nabla x A = B \tag{3.41}$$

and the eddy current density (J_e) is computed using equation (3.42)

$$J_e = -j\omega\sigma A \tag{3.42}$$

CHAPTER 4. PROBABILITY OF DETECTION (POD) MODELS FOR NDE TECHNIQUES

4.1. Introduction

In most NDE applications the inspection systems are generally driven to their extreme capability in detecting the smallest of the flaws. For instance one major concern in the aircraft industry is the detection of Multi-Site Damage (MSD) that occur in aging aircrafts. The MSD is caused by fatigue and generally occurs in lap-joints in older commercial airplanes. As shown in Figure 4.1 the phenomenon is characterized by small, longitudinal cracks

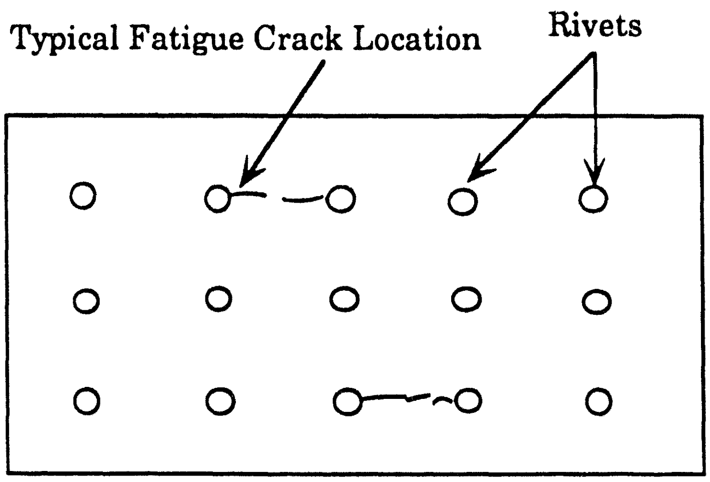

Figure 4.1: Figure showing a simple Multi-Site Damage

between successive rivet joints. These and many other types of tight cracks are often very difficult to be detected by NDE techniques. Moreover the detectability of a flaw by a chosen NDE technique depends upon the geometry, type of flaw and other testing conditions. Consequently a flaw easily detected by one method will not be detected at all by another NDE procedure. Also using a single inspection system, repeated scans of the same flaw will not result in the detection of the flaw each time due to a number of factors that influence the measurement. These factors contribute to variations in the measured value. For instance the variabilities in the eddy current NDE inspection system are due to several factors such as human factors, liftoff, material conductivity and permeability, probe canting angle, surface roughness, temperature, scan related factors and so on. The effect of these factors on a signal can be expressed as

$$\text{Measured Signal} = \text{Flaw Signal} + \text{Noise} \tag{4.1}$$

Under these conditions, signals generated by identical flaws or alternatively signals obtained by repeated scans of the same flaw are seldom the same and flaws of the same nominal size will produce signals spanning a range of values. Therefore a flaw of a given size, 'a', will result in a distribution of the signal amplitude when measured over a population of components containing such defects. In Figure 4.2 the measurement variable, y, is plotted on the Y axis and the flaw variable on the X axis. For a certain flaw size x_1, the measurement variable has a distribution with mean y_1 and a certain variance. At a different flaw size, x_2, the measurement variable has a similar distribution with a different mean, y_2. In the eddy current test as the flaw size x increases the mean of the corresponding distribution increases, as is seen in Figure 4.2 where $p(y/x_1)$ and $p(y/x_2)$ are the conditional probability density functions of the measurement variable y at the flaw sizes x_1 and x_2 respectively. Due to this uncertainty in the measured value the capability of the inspection process is characterized in terms of the probability of detection (POD) of a flaw, usually the critical flaw.

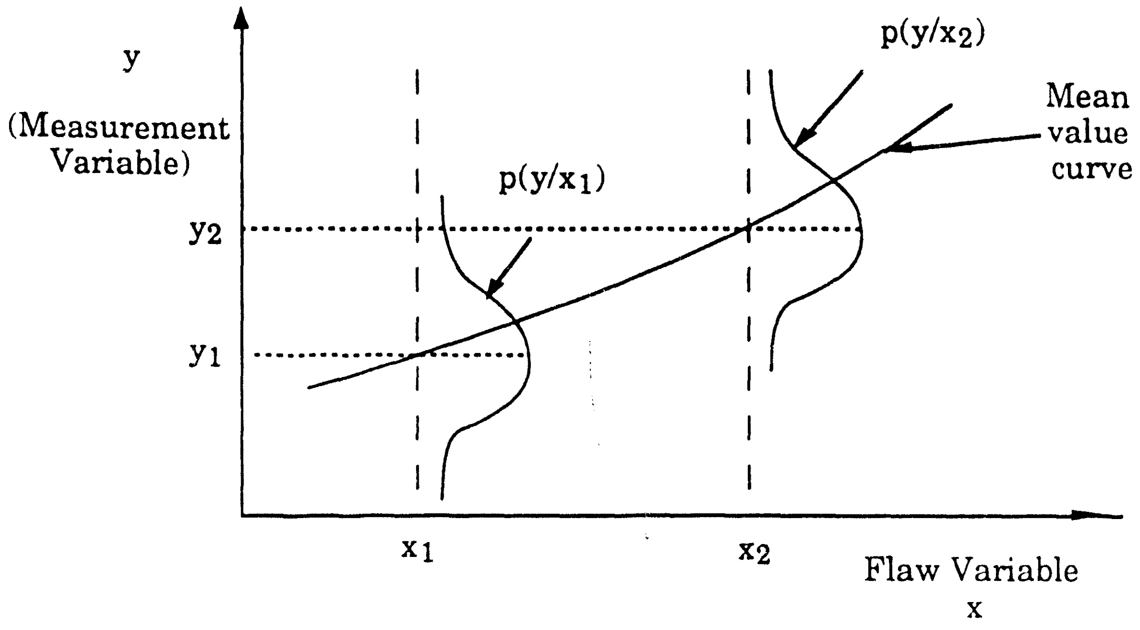

Figure 4.2: The distributions of the peak amplitude of the signal at two different flaw dimensions

Hence there is a need for developing probability of detection models. These models are also useful for assessing the applicability of a particular technique. Since the POD depends on the test conditions such as geometry and orientation of the flaws, these models can be used for obtaining a measure of performance of different NDE techniques for a particular application. In addition, the test parameters can be optimized in order to achieve the highest probability of detection for a given critical flaw.

4.2. POD Models

4.2.1. Introduction

The main objective in nondestructive evaluation is to make an accept-reject decision based on the absence or presence of a flaw respectively in the inspected part. However there are a number of other secondary factors involved in the accept-reject decision process such as the cost incurred due to the false acceptance (flawed component accepted) and false alarm (unflawed component rejected) rates that affect the decision process. Due to these factors, over the years a number of approaches have evolved in the NDE methodologies including the probabilistic techniques. The three main approaches in this development, can be characterized as [31] zero-defects, deterministic and probabilistic and are explained in more detail next.

4.2.2. Zero Defects Approach

In this approach the material is rejected if a flaw is present and accepted otherwise. However, in a practical situation, very small defects may go undetected and hence this results in rejection of a component only if a detectable defect is present. Figure 4.3 gives a schematic representation of this process. As seen in Figure 4.3 the test results in two states: $Y = 0$ or 1 corresponding to no detection or detection of the flaw respectively.

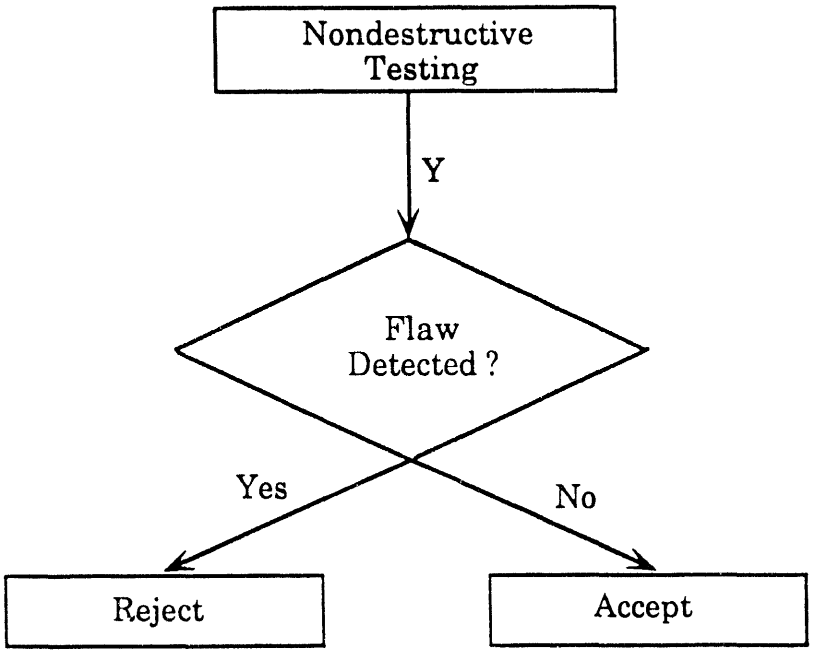

Figure 4.3 [31]: Zero defects decision process

This type of data is also called hit/miss data and an analysis method for this type of data is explained in [32-36]. In order to estimate the POD of a flaw from the hit/miss data a mathematical model for POD(a), where 'a' is the flaw size, was devised in recent years. Seven different functional forms were tested [33] for applicability to the inspection data and the log-logistics (log odds) function was found to provide the most optimal model. Two equivalent mathematical forms of this model have been used. The first form was given by

$$\mathrm{POD}(a) = \frac{\exp(\alpha + \beta \ln a)}{1 + \exp(\alpha + \beta \ln a)} \tag{4.2}$$

and the second, equivalent, form representing POD(a) is

$$\ln\left[\frac{\mathrm{POD}(a)}{1 - \mathrm{POD}(a)}\right] = \alpha + \beta \ln(a) \tag{4.3}$$

The parameters of this function α and β can be estimated using maximum likelihood methods. The log odds model is commonly used in the analysis of the hit/miss data because of its analytical tractability. Once the parameters are estimated one can compute the POD of a flaw of size 'a'.

The problem with the zero defects approach is that as the NDT techniques evolve, smaller and smaller flaws will become detectable. While this results in smaller false acceptance rates it also leads to high false alarm rates which is highly undesirable. If the sensitivity of the NDT system is low this procedure is acceptable, however if the system is highly sensitive the decision process will result in very large false alarms.

4.2.3. Deterministic Approach

A schematic representation of this approach is given in Figure 4.4. This approach overcomes some of the deficiencies of the earlier approach by the introduction of a fracture mechanics model. The fracture mechanics model determines the shape and size of the crack and a decision as to whether this crack would lead to failure of the material under the worst case stress

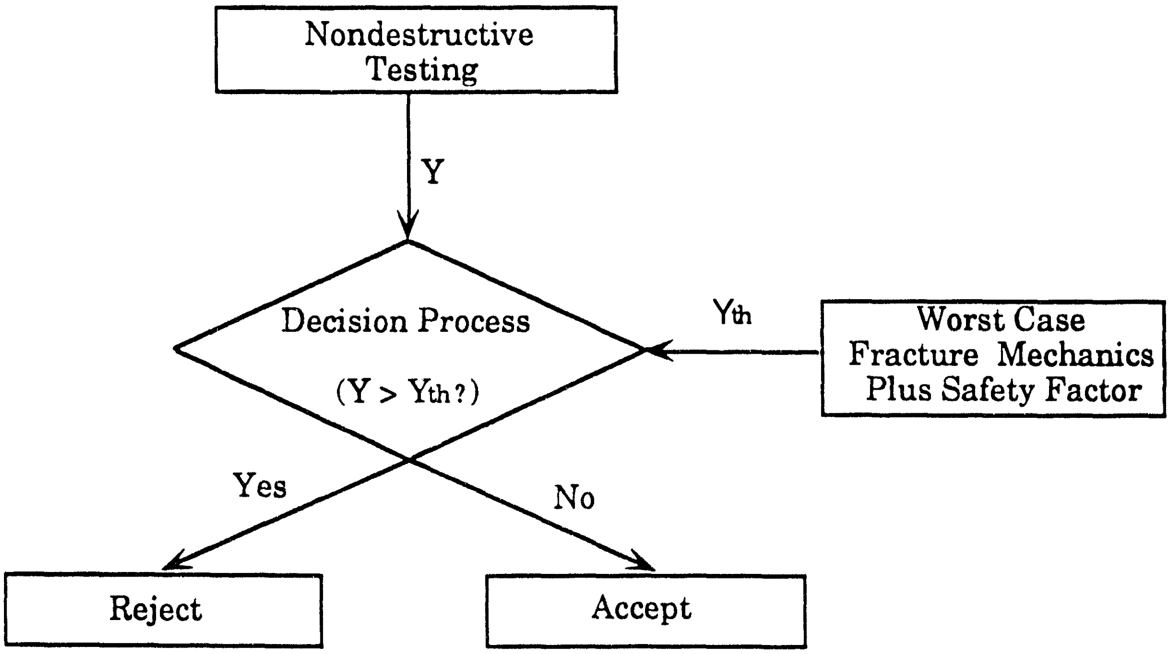

Figure 4.4 [31]: Deterministic decision process

environment. This provides a threshold, corresponding to the critical flaw size used during the decision process, which in turn controls the false alarm rates even with increased sensitivity of the NDT system. However in general the failure process is not deterministic and hence there could be failure of the material even when the deterministic theory predicts the contrary. Moreover due to various statistical variations involved in the nondestructive testing process, a safety factor is incorporated along with the fracture mechanics model in order to avoid a high probability of failure. Unfortunately, in the absence of probabilistic models, no proper procedure for the determination of the safety factor exists since not much data is available at acceptable failure rates.

4.2.4. Probabilistic Approach

The third approach in the development in the NDE methodologies involves the determination of the probability of detection of a given flaw using the optimum accept-reject decision criterion. This approach also takes into consideration various statistical perturbations occurring during the measurement process. The probabilistic approach has been used in this thesis and the concepts involved are explained in more detail in the next section.

4.2.5. POD Concepts

The probability of detection of a particular flaw of a given size using a given measurement system can be determined by generating conditional probability density functions (PDFs) of the measurement signal shown in Figure 4.2. Figure 4.5 shows the distributions of the peak amplitude of the signal in the absence of a flaw, $p(y/x_0)$, and in the presence of a flaw, $p(y/x_1)$.

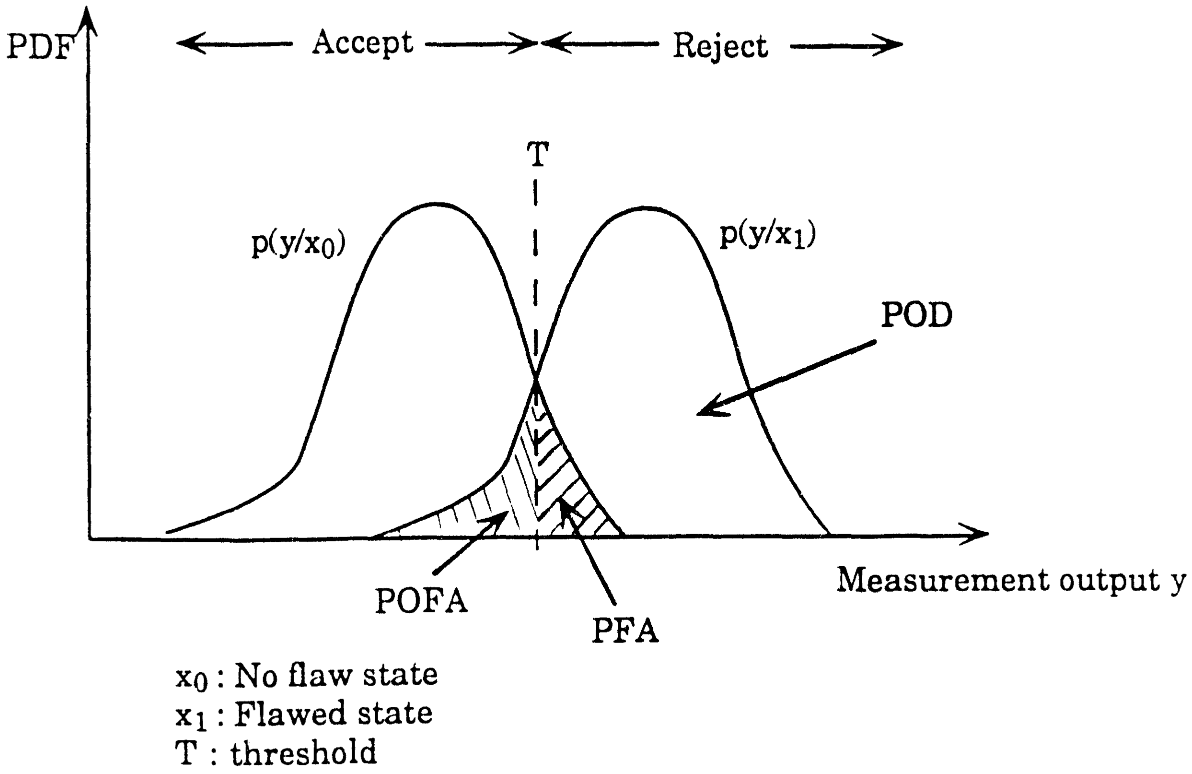

Figure 4.5: The distributions of the peak amplitude of the signal without a flaw and in the presence of a flaw

The interpretation of NDT data involves the decision as to whether the observed response is a flaw signal or noise (no flaw signal). The simplest approach to making this decision is to choose a threshold signal level (T) such that all signals above the level will be classified as flaw signals and all signals below the level will be interpreted as noise. If the signal and noise probability density functions overlap, as shown in Figure 4.5, the data interpretation based on threshold detection will inevitably involve two types of errors which are of significance. The two types of errors are:

1. False alarm: The components with no flaw are rejected due to incorrect interpretation of noise fluctuations as a flaw indication. The probability of such an incorrect interpretation is called the probability of false alarm (PFA). From economic considerations a high false alarm rate is undesirable as this would result in the unnecessary replacement of components which are actually in good condition.
2. False acceptance: This is caused by the acceptance of the material with a flaw which actually needs to be replaced, due to a miss in the detection of the flaw. The probability of such an incorrect interpretation, (1 - POD), is called the probability of false acceptance (POFA). This could result in very serious consequences and is a very important factor particularly in aircraft and nuclear power industries.

Given the signal and noise PDFs, one can determine how the POD and the PFA, of a flaw, depend on the choice of the threshold signal. As illustrated in Figure 4.5 the POD is the area to the right of the threshold under the signal PDF curve and is mathematically represented by

$$\mathrm{POD} = \int_{T}^{\infty} p(y/x_1)\,dy \tag{4.4}$$

while the PFA is the corresponding area under the noise PDF and is defined mathematically by

$$\mathrm{PFA} = \int_{T}^{\infty} p(y/x_0)\,dy \tag{4.5}$$

The probability of false acceptance of the inspected part is equal to (1 - POD) and is represented by

$$\mathrm{POFA} = \int_{-\infty}^{T} p(y/x_1)\,dy \tag{4.6}$$

As the flaw size becomes smaller and smaller the mean of $p(y/x_1)$ decreases resulting in the shifting of $p(y/x_1)$ towards the left. This increases the overlap between the two distributions and the corresponding POD of the flaw is reduced. On the contrary as the flaw size increases the $p(y/x_1)$ shifts towards the right, the overlap between the two distributions decrease and the POD of the flaw increases as expected.

By choosing a number of different threshold values, one can generate a set of ordered pairs of POD and PFA values, which provides the relative operating characteristics (ROC) of inspection for the flaw. The relative operating characteristics shows the POD that can be achieved for a certain

PFA. As an example Figure 4.6 shows the ROC of an aircore probe scanning the surface of a specimen with a flaw. The specimen material is Aluminum AL2024 and the dimensions of the axisymmetric flaw are 0.1 mm width and 0.25 mm depth. The frequency of operation is 500 KHz. In the operating characteristics of Figure 4.6 it is seen that if the threshold signal is such that the PFA is 0.927, then the corresponding detection probability of the flaw is 0.984, and at a different threshold giving PFA of 0.108, the POD is 0.321.

Various probabilistic approaches (models) are being currently used for estimating the probability of detection of a flaw. Some of the commonly used approaches are listed below.

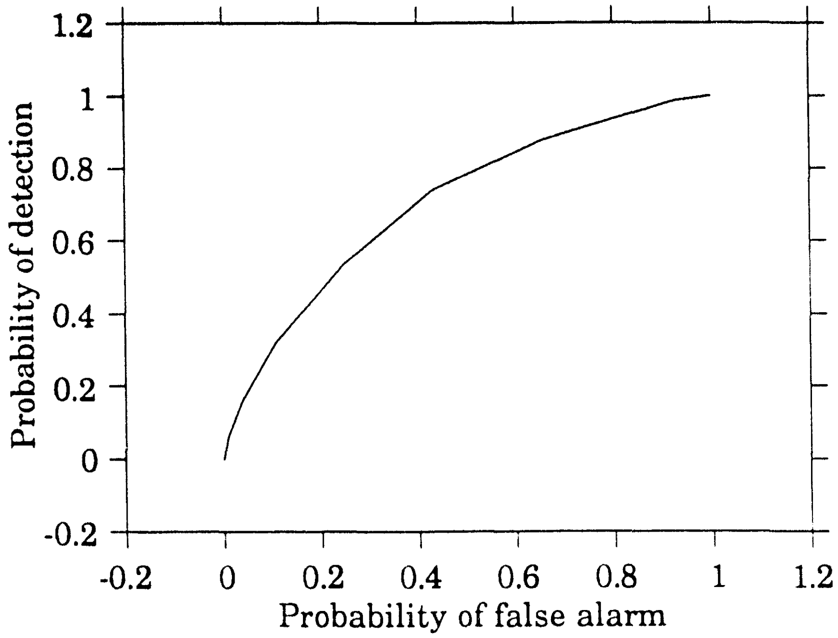

Figure 4.6: Relative Operating Characteristics of an aircore probe at 500 KHz

1. Experimental Model - In this approach the flaw signals and their fluctuations are determined by using a large number of sample measurements over a variety of flaws. A study of the experimental approach for determining the probability of detection of a flaw has been dealt with in [37]. This technique involves a number of inspectors testing a large number of flawed specimens. The experimental data is used to estimate the POD of the flaw. Unfortunately the determination of the probability of detection of defects requires a rather extensive set of measurements to obtain statistically sound estimates. In general this approach, for generating POD curves, is time consuming and expensive particularly since it involves the machining of difficult defect shapes in a large number of samples and also requires large number of operators.

2. Theoretical Model (Model based POD) [38,39,40] - The limitations of the experiment based POD prediction is overcome by simulating on a digital computer the measurements one would make in an experimental set up. The flaw signal and the effect of measurement variabilities are predicted by the computer model. In general, this approach requires reliable methods for predicting flaw signals and background noise as a function of flaw size and shape, probe configuration and other inspection parameters. The model based POD estimates, unlike the purely experimental approach, leads to significant cost benefits.

3. Hybrid Model - This model uses a combined theoretical and experimental approach. Theoretical predictions help in determining flaw signals and a

certain amount of experimental data is used to account for the noise parameters.

This thesis deals with the study of the model based POD and its application for the estimation of the POD for eddy current NDT. Figure 4.7 gives a schematic representation of the model based POD. At the heart of the figure is the measurement model. The inputs to the measurement model are

1. The representation of the component from a CAD package.
2. The critical flaw information from a fracture mechanics model and
3. Measurement variabilities and measurement noise.

The measurement model combines all these inputs to generate a conditional probability density function of the measurement variable y for the flaw size x. Once such PDFs for the no flaw and the flawed states are generated the parameters of interest like probability of detection and probability of false alarm are computed. In this thesis the finite element model for eddy current NDT serves as the measurement model to predict the flaw signals, in a given test geometry. The stages involved in the POD estimations for the eddy current NDT are explained in more detail in the following sections.

4.3. Model Based POD estimation for Eddy Current NDT

Figure 4.8 shows a block diagram for model based estimation of POD in eddy current inspections. The major steps involved in the procedure are described next.

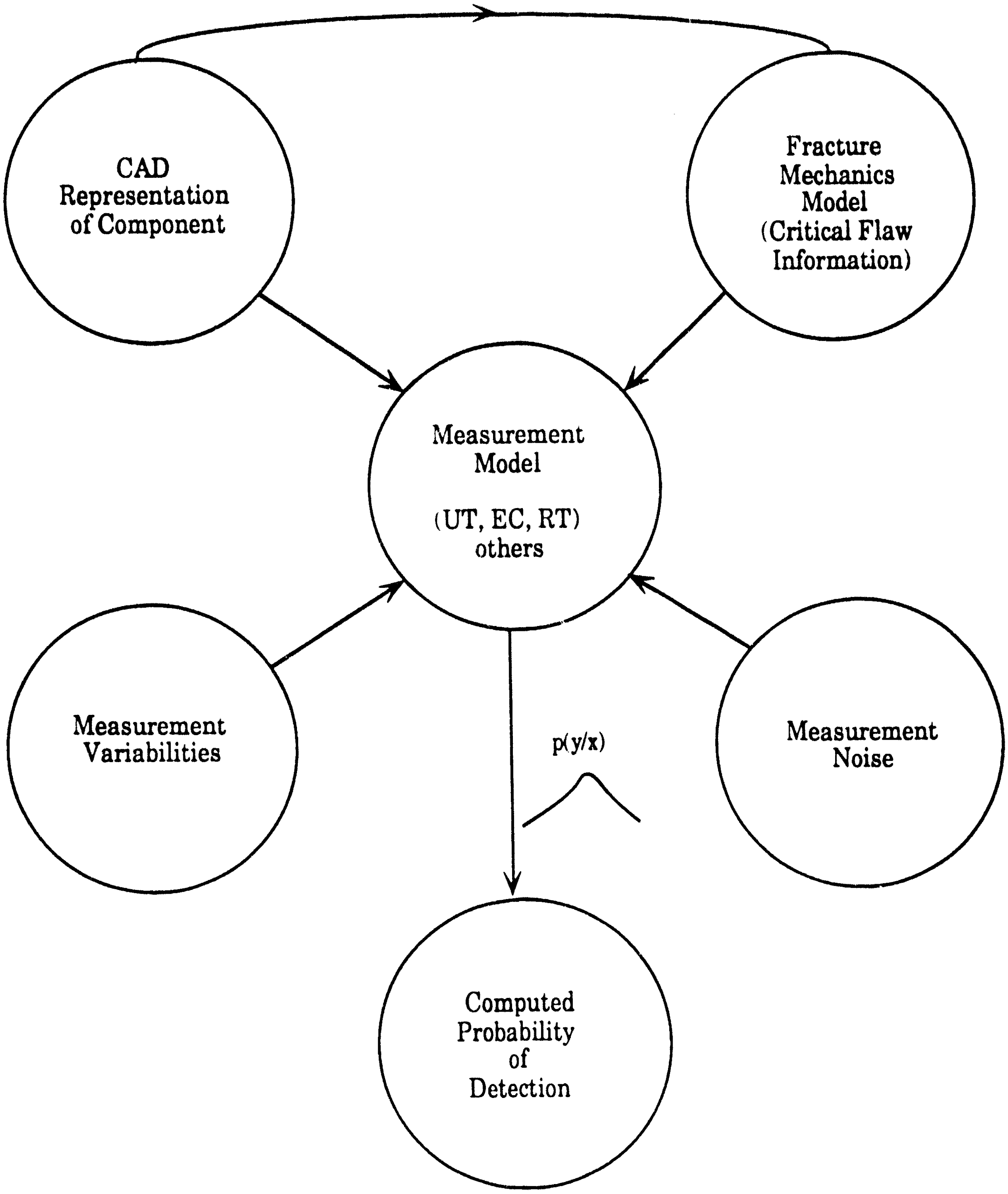

Figure 4.7: A schematic representation of model based POD estimation

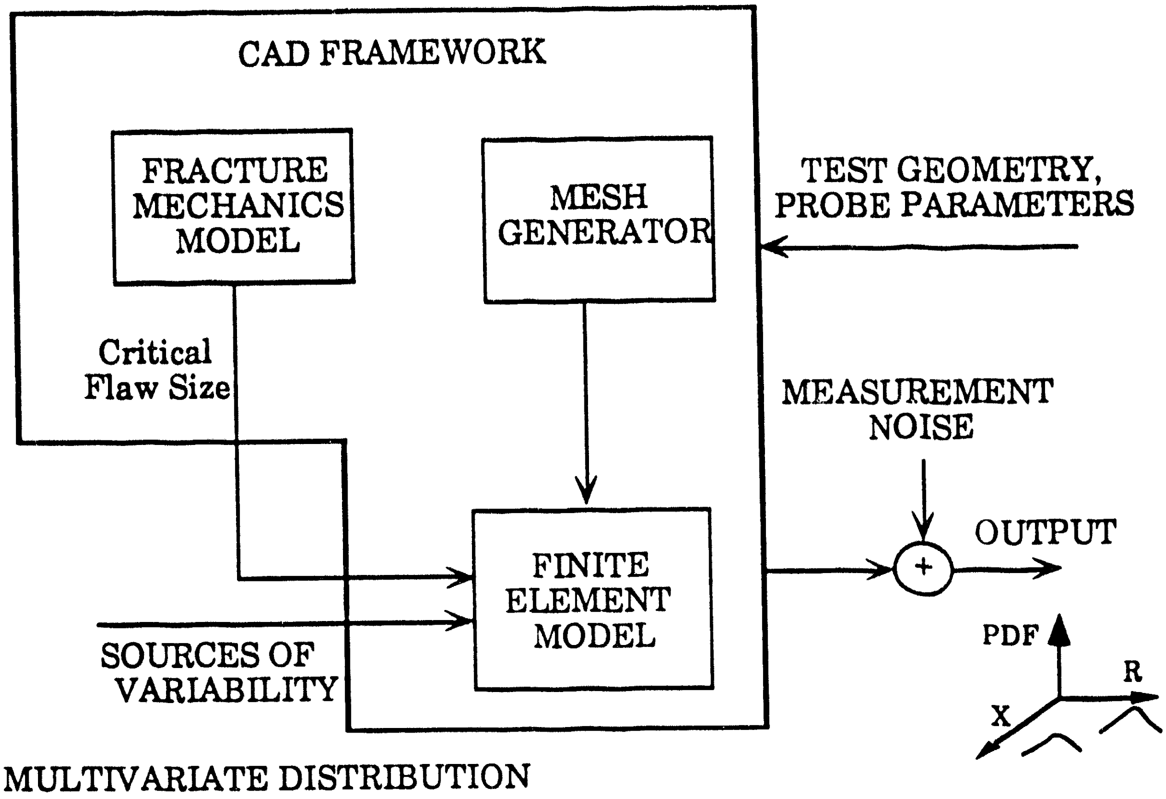

Figure 4.8: A schematic representation for POD estimation in eddy current NDT

4.3.1. Step 1 : Sources of Variability

The sources of variabilities in the eddy current NDT are due to several factors, as shown in Figure 4.9. These sources include:

1. Human factors,
2. Part geometry
3. Material property variations
    i. Conductivity
    ii. Permeability

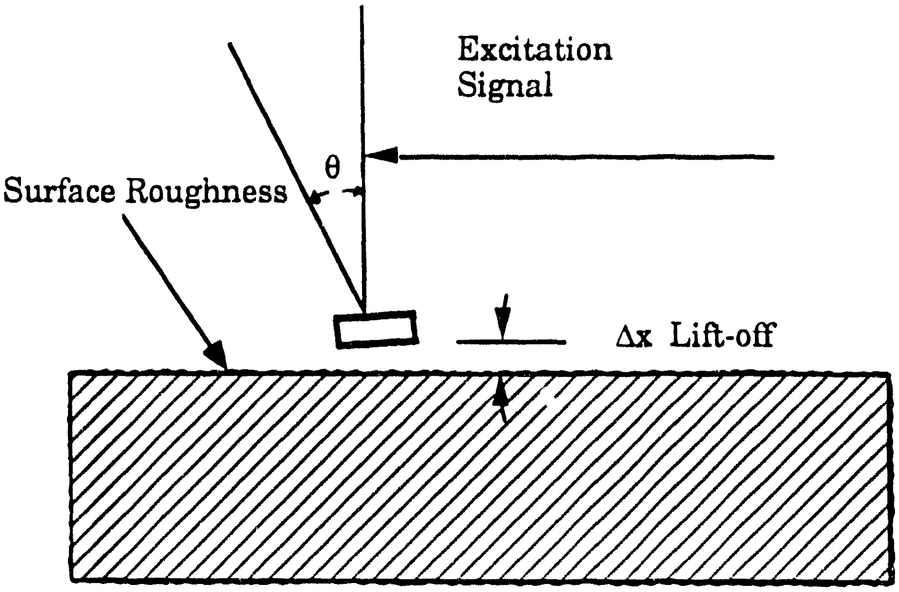

Figure 4.9: Sources of variabilities in the eddy current NDT System

4. Physical factors
    - i. Surface Roughness
    - ii. Lift-off variations
    - iii. Temperature variations
    - iv. Probe canting angle θ
    - v. Scan related factors
5. Instrumentation Noise

A statistical model is used for characterizing both the individual and simultaneous occurrence of the above mentioned variabilities. Individual variations, is incorporated by the use of a univariate Gaussian random number generator with a certain mean and variance. The statistical model uses a multivariate random Gaussian number generator to combine the multiple measurement variations into a multivariate Normal distribution N(μ,Σ) where μ is the mean vector containing the {mean liftoff, mean conductivity, mean surface roughness ....} and Σ is the diagonal covariance matrix. The parameters of the input distribution can be adjusted using experimental measurement conditions.

4.3.2. Step 2 : Generation of the Signal Probability Density Functions (PDFs)

The procedure for generating the conditional PDFs for a given flaw, under the influence of the various variabilities listed above, is summarized in Figure 4.10. The test parameters contain information regarding the critical

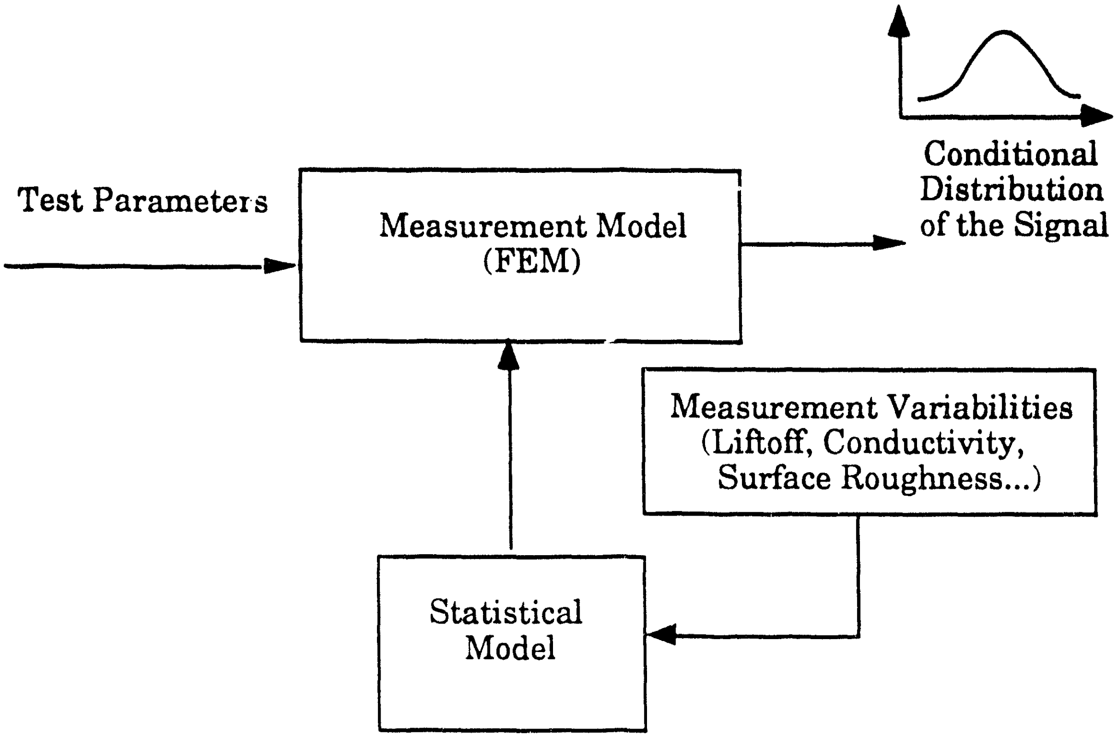

Figure 4.10: Inputs to the finite element model (FEM) for POD estimates

flaw size and the experimental setup geometry. The measurement model is simulated repeatedly with the perturbations and the output of the measurement model gives the conditional probability density function of the signal amplitude.

As an example, an aircore probe scanning the surface of a material (AL 2024) with an axisymmetric flaw of cross-section 0.25 mm x 0.25 mm was modeled using a 2D axisymmetric finite element model (FEM). Figure 4.11 shows the PDFs for the noise and the flawed signals generated with the measurement model perturbed with the liftoff variability alone.

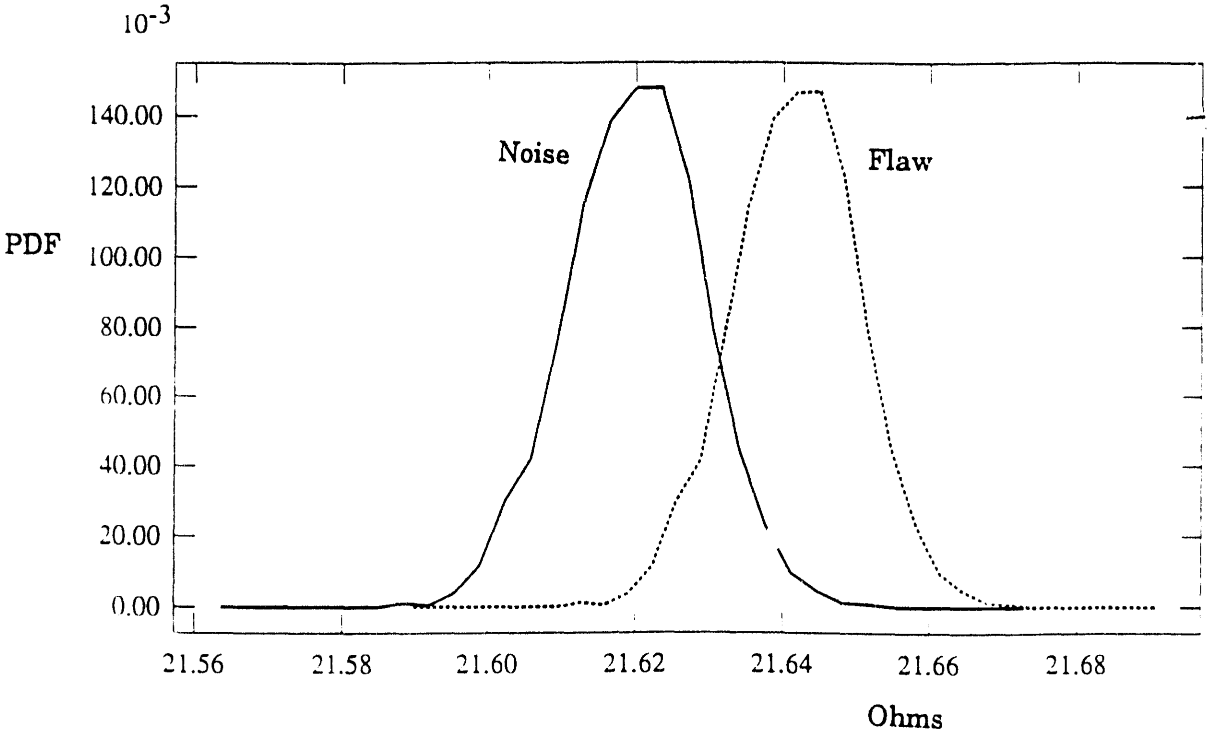

Figure 4.11: PDFs for the no flaw and flawed states with the liftoff variability acting on the test system

4.3.3. Step 3: Selection of the Threshold

Once the PDFs are obtained, the threshold T is then selected using an appropriate criterion. The selection of the threshold is a very important factor in signal classification. As seen in Figure 4.5 the detection probability of a flaw is dependent on the value of T chosen. As the threshold value decrease the POD of the flaw increase along with an increase in the false alarm (PFA) rate. Various criteria can be used for selecting the threshold based on the application problem. Three of these criteria investigated in this thesis are:

1. Set PFA to a constant: In many applications of interest to industry it is desired to keep the probability of false alarm as low as possible. The PFA is dependent only on the PDF of the background noise and is independent of the PDF of the flaw signal. The threshold is selected such that PFA is set at a prescribed value θ1.

2. Set POD of the critical flaw size to a constant: When the inspection system is required to detect only flaws that are bigger than a critical size the threshold can be chosen such that the critical flaw is detected with a specified POD, θ2, and this threshold is used to compute the PFA and POD of other flaws of different dimensions.

3. Minimization of the total signal classification error (Method of mixtures) [39,41]: As explained earlier, the PFA and POFA, in Figure 4.12, representing the false reject and false acceptance of the inspected part, are the error probabilities of the signal interpretation. The threshold T can also be selected to

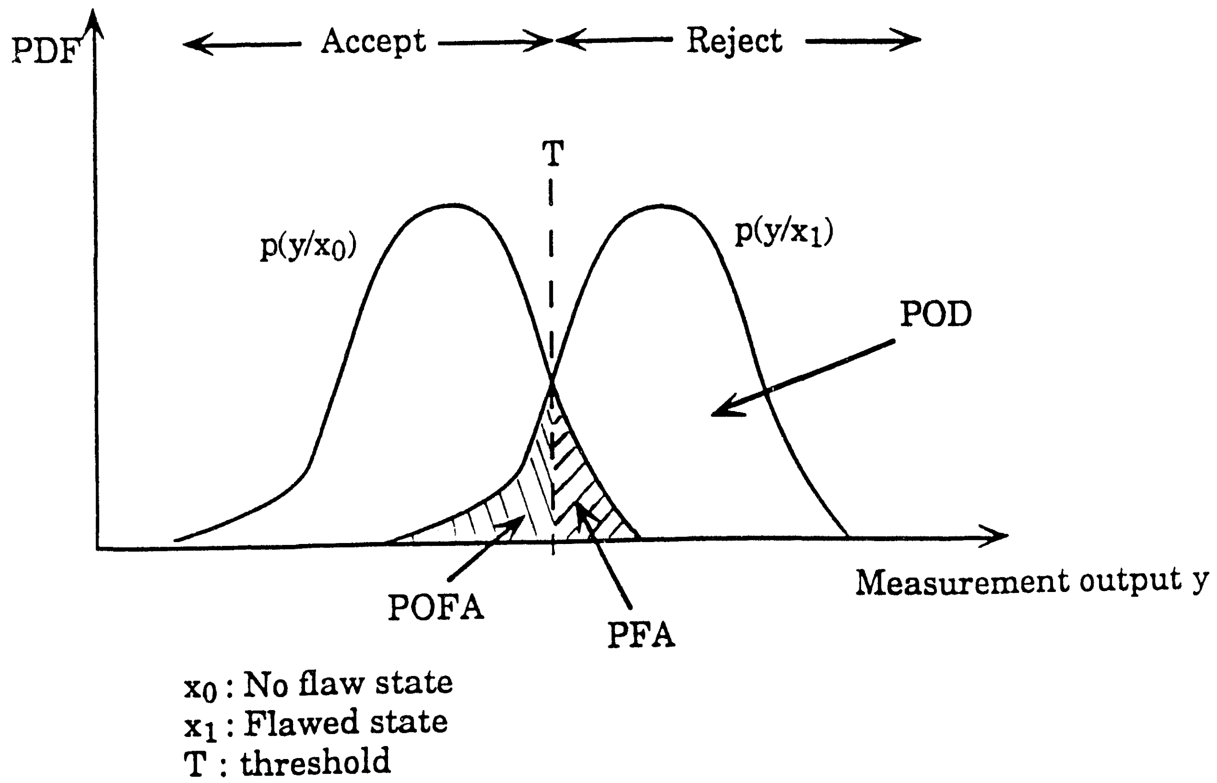

Figure 4.12: The distributions of the peak amplitude of the signal without a flaw and in the presence of a flaw

minimize the weighted sum of the overall error in signal classification using the method of mixtures. In this approach the resultant signal distribution is modeled as a weighted mixture of the two distributions for the no flaw and flawed states given by

$$p(y) = a.\ p(y/x_1) + (1-a).\ p(y/x_0) \tag{4.7}$$

where 'a' is the probability of a flaw being present in the region of interest.

For a given T the two error probabilities are given by equations

$$E_1(T) = \int_T^{\infty} p(y/x_0)\, dy \qquad \text{(PFA)} \tag{4.8}$$

$$E_2(T) = \int_{-\infty}^{T} p(y/x_1)\, dy \qquad \text{(POFA)} \tag{4.9}$$

This results in the weighted sum of the overall signal classification error

$$E(T) = a\ E_2(T) + (1\text{-}a)\, E_1(T) \tag{4.10}$$

The minimization of the weighted sum of the overall signal classification error E(T) with respect to T yields

$$\frac{\partial E(T)}{\partial t} = 0 \tag{4.11}$$

The threshold T is obtained from the solution of equation 4.11.

4.3.4. Step 4: Calculation of the Parameters of Interest

Once the threshold, T, is selected the final step is to compute the parameters of interest such as the probability of detection and probability of false alarm, given by equations (4.4) and (4.5), of the flaw. Basically this involves the integration of certain regions of the probability density functions, of the measurement variable, in the presence and absence of the flaw. The integration is carried out using a Monte Carlo simulation technique and the estimated value is given by the ratio

$$N_p/N \tag{4.12}$$

where N_p is the total number of samples in the region of interest and N the total number of samples in the distribution.

The POD model can also be used to generate the relative operating characteristics curve of the system for a flaw. Once the PDFs in the absence and presence of the flaw are generated, the probability of detection and probability of false alarm values for a number of threshold levels are computed. A plot of the PFA vs POD for the different values of threshold represent the ROC curve of the system for the flaw.

Also the model can be used to generate POD curves for flaws of varying widths. PDFs for the different flaws of varying widths and a constant depth are generated and the threshold selected using one of the criteria. The PODs for the various flaws are then computed using this value of the threshold and plotted in the POD curve.

Results demonstrating the feasibility of the model based POD technique including the generation of the ROC and POD curves for an eddy current nondestructive testing system are presented in the next chapter.

CHAPTER 5. SIMULATION RESULTS AND DISCUSSIONS

5.1. Introduction

The POD model for eddy current NDT described thus far, was exercised using an axisymmetric two dimensional finite element code. The variabilities associated with the measurement process were considered individually using a univariate Gaussian representation. Simultaneous perturbation of multiple parameters was also modeled using a multivariate Gaussian distribution with an appropriate mean vector and covariance matrix. The POD model simulations results in the generation of the conditional PDFs of the background noise as well as flaw signals of varying size. Thresholds were selected using different criteria, explained in chapter 4, and the detection probability of the flaws, using these thresholds, were computed. Results demonstrating the feasibility of the model based POD estimations of a flaw are presented.

A brief description of the procedure for the generation of normal variates is given in Appendix. Some definitions of the parameters used for analyzing the various distributions are described. The number of independent samples, N, required for estimating the probabilities with the desired accuracy is derived first.

5.2. Confidence Interval for the Estimation of POD

The PDFs of the measurement variable in the presence and absence of a flaw are used for calculating the parameters of interest such as probability of detection, probability of false alarm and probability of false acceptance by integrating the density functions. For instance, Figure 5.1 shows typical PDFs in the presence and absence of a flaw. The probability of detection, described in equation (4.4), is the integration from the threshold, T, to infinity of the flaw signal PDF. This parameter is estimated using the Monte Carlo simulation technique which involves the summation of the total number of times the

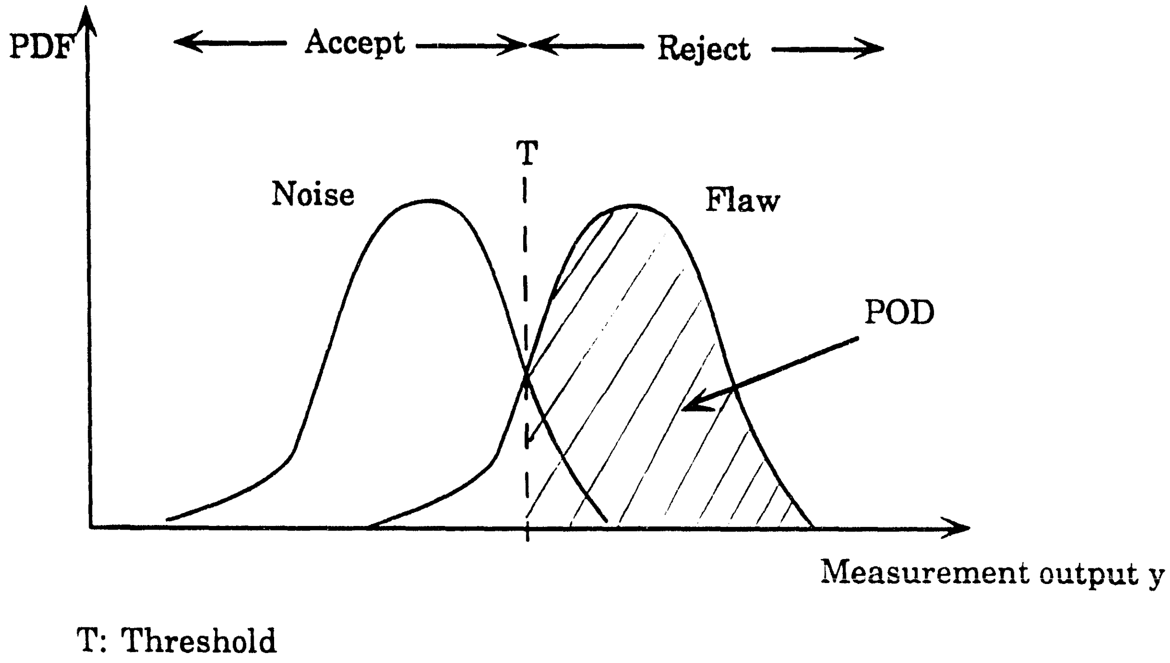

Figure 5.1: Typical noise and flaw PDFs

samples fall in the region of interest in the distribution. Let $\hat{P}_k$ be the estimated value of the parameter whose true value is P_k. The estimate of the POD, $\hat{P}_k$, can be represented by

$$\hat{P}_k = \frac{N_p}{N} \tag{5.1}$$

where N_p is the total number of samples in the region of interest and N the total number of simulations.

As N is increased, the accuracy of the estimates get better. One can therefore calculate a confidence interval for the estimated probabilities. By applying Chebyshev's inequality, for any $\varepsilon > 0$, we can obtain a probabilistic bound on the accuracy of this estimate given by

$$P(|\hat{P}_k - P_k| > \varepsilon) \leq \frac{E[(\hat{P}_k - P_k)^2]}{\varepsilon^2} \tag{5.2}$$

Let X_1, X_2 .... X_N, be the N samples in the distribution. From equation (5.1) $\hat{P}_k$ can be given by

$$\hat{P}_k = \frac{\sum_{k=1}^{N} I_k}{N} \tag{5.3}$$

where I_K is the indicator function defined as

I_k $=1$ if X_k falls in the region of interest

$= 0$ otherwise.

$$E(I_k) = 1.\,[\,P(I_k = 1)\,] + 0.\,[\,P(I_k = 0)\,]$$
$$= P_k \qquad (5.4)$$

$$\mathrm{Var}\,(I_k) = E\,(I_k{}^2) - (E\,(I_k))^2$$
$$= P_k - P_k{}^2$$
$$= P_k\,(1 - P_k) \qquad (5.5)$$

From equations (5.3) and (5.4) we get

$$E\,(\hat{P}_k) = \frac{\sum_{k=1}^{N} E\,(I_k)}{N} = \frac{N\,.\,P_k}{N} = P_k \qquad (5.6)$$

From equations (5.3) and (5.5) we get

$$E\,[(\hat{P}_k - P_k)^2] = \mathrm{Var}\,(\hat{P}_k) = \frac{\sum_{k=1}^{N} \mathrm{Var}\,(I_k)}{N^2}$$

$$= \frac{N.\,P_k\,(1 - P_k)}{N^2} = \frac{P_k\,(1 - P_k)}{N} \qquad (5.7)$$

Since (5.7) is maximized at $P_k = \frac{1}{2}$, we have $E\,[(\hat{P}_k - P_k)^2] \le \frac{1}{4N}$.

Thus from equations (5.2) and (5.7) we have

$$P(\,|\hat{P}_k - P_k| > \varepsilon\,) \le \frac{1}{4N\varepsilon^2} \qquad (5.8)$$

If the sample size, N, is 2500 and we set $P(|\hat{P}_k - P_k| > \varepsilon)$ to 0.05 we have

$$0.05 \leq \frac{1}{4 \times 2500\, \varepsilon^2}$$

$$\varepsilon \leq 0.0447 \tag{5.9}$$

In other words we can assert with 95 % confidence that with a sample size of 2500, the error in the estimated value is in the interval (- 0.0447, + 0.0447).

5.3. Definitions of the Distribution Parameters [42]

The distribution parameters such as the mean, standard deviation, coefficient of skewness and kurtosis, used for analyzing the signal probability density functions are defined below.

The mean, μ, of a population of N variables $\{ X_1, X_1 \ldots\ldots\ldots X_N \}$ is given by

$$\mu = \frac{1}{N} \sum_{i=1}^{N} X_i \tag{5.10}$$

The standard deviation, σ, is defined as

$$\sigma = \sqrt{E\left[(X - \mu)^2\right]} = \sqrt{\frac{\sum_{i=1}^{N} (X_i - \mu)^2}{N}} \tag{5.11}$$

When a distribution is not symmetrical about its mean the distribution is said to be skewed. A measure of this asymmetry is given by the coefficient of skewness (SK) defined as

$$SK = \frac{\sum_{i=1}^{N} (X_i - \mu)^3}{\sigma^3} \tag{5.12}$$

If the coefficient, SK is zero then the distribution is symmetrical about its mean. However a positive coefficient of SK indicates that there are more number of samples occurring to the right of the mean.

The kurtosis involves the fourth order moment and gives the degree of flatness of the distribution. This parameter is defined as

$$\text{Kurtosis} = \frac{\sum_{i=1}^{N} (X_i - \mu)^4}{\sigma^4} \tag{5.13}$$

While comparing two distributions, a higher kurtosis value implies that the distribution has a sharper peak indicating the occurrence of more samples near the mean of the distribution. On the other hand a smaller value of kurtosis indicates that the distribution is flatter.

5.4. Monte Carlo Simulation

The probability density function of the eddy current signal is generated by perturbing the finite element measurement model using measurement variations represented by univariate or multivariate Gaussian distributions. As a first step towards this process the numerical model was validated by comparing with experimental values.

5.4.1. Validation of the Finite Element Model

The finite element model was first validated by comparing the model prediction to the experimental measurement. The geometry of the experimental setup consists of an absolute aircore eddy current probe scanning the surface of an aluminum plate. The material used was AL 2024. The dimensions of the probe are as shown in Table 5.1. The frequency of the

Table 5.1. Parameters of the eddy current aircore probe

Inside diameter (mm)	1.07
Outside diameter (mm)	2.62
Mean coil radius (mm)	0.92
Coil length (mm)	2.93
Liftoff height (mm)	0.56
Number of turns	235

excitation current in the probe was 500 KHz. An axisymmetric flaw, in the from of a pit, of diameter 0.77 mm and depth 0.4 mm was then machined in the material. The geometry and material properties was input to the finite element model. The probe impedance in the presence and absence of the flaw was predicted and compared to the experimental data. These results are summarized in Table 5.2. The model predictions were within 1% of the experimentally measured value.

Table 5.2. Results demonstrating the experimental validation of the 2D axisymmetric finite element model

Condition	$\lvert Z \rvert_{\text{Model}}$ (Ohms)	$\lvert Z \rvert_{\text{Experiment}}$ (Ohms)
No flaw	110.5821	111.190
With flaw	110.5845	111.1919

5.4.2. Effect of Single Sources of Variability

In the first test, the individual variations in liftoff, material conductivity and surface roughness were considered using univariate normal distributions. The effect of these variations was observed by perturbing the measurement model using appropriate univariate random normals. The dimensions of the flaw cross-section was chosen to be of 0.25 mm width and 0.25 mm depth. The corresponding model predictions were used to generate the conditional PDFs of the measurement variable in the presence and absence of the flaw. The measurement variable is the peak value of the magnitude of the probe impedance. These PDFs are shown in Figures 5.2 to 5.4.

At first glance the flaw signal distribution appears to be a shifted version of the noise distribution. In order to look more closely at the influence of the variations, on the eddy current measurements, the parameters of the distributions were calculated. The parameters of the input distributions used

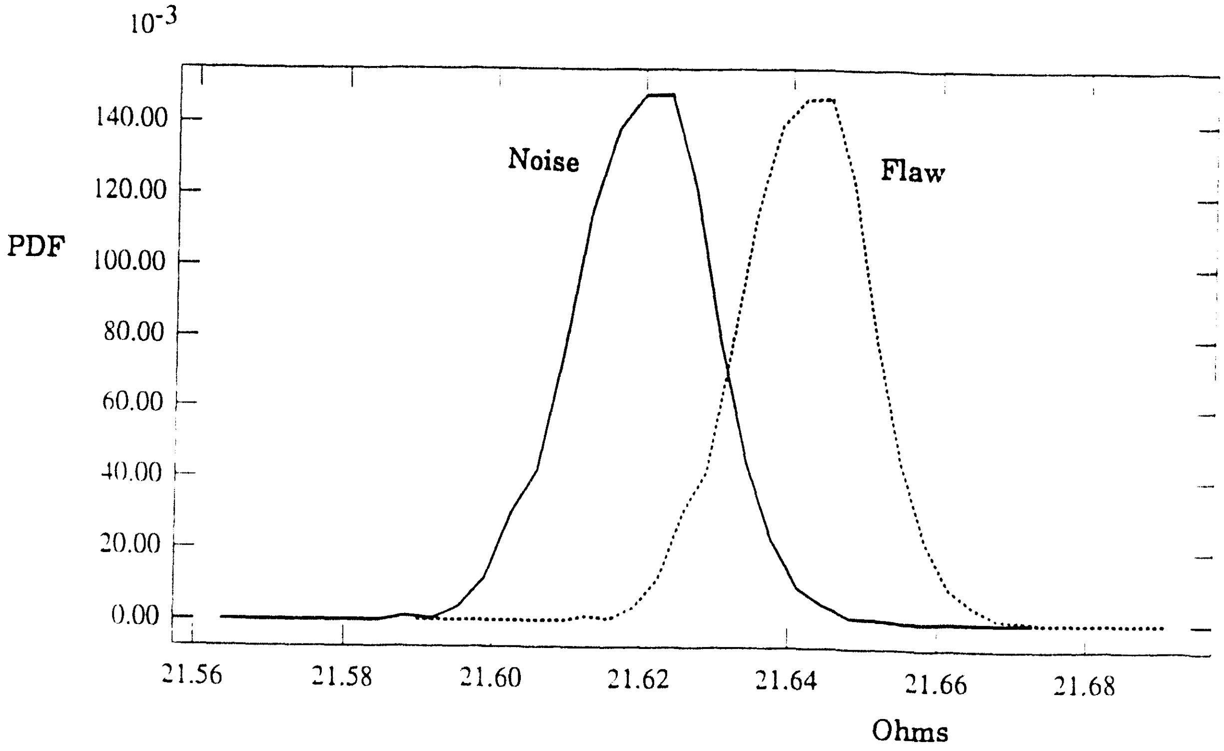

Figure 5.2: PDFs for the noise and flaw signal due to liftoff variations

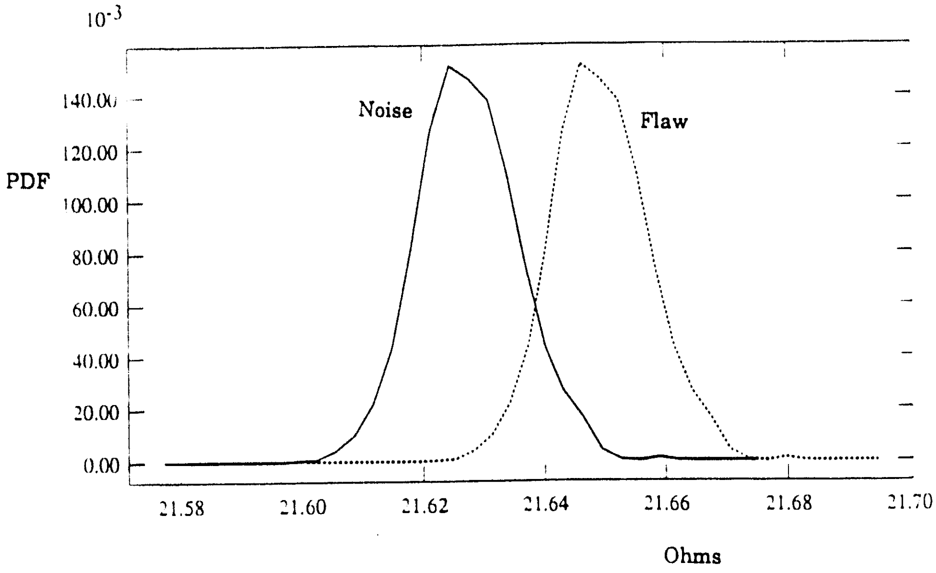

Figure 5.3: PDFs for the noise and flaw signal due to conductivity variations

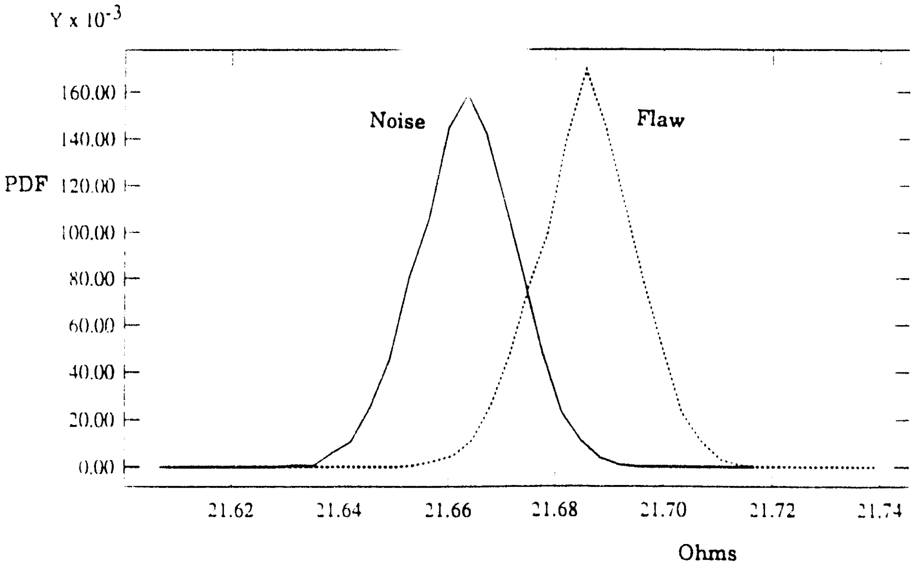

Figure 5.4: PDFs for the noise and flaw signal due to surface roughness variations

for perturbing the measurement model are summarized in Table 5.3. The parameters of the distributions of the model predicted signals are reported in Table 5.4. It is seen that as long as the variance of the input distribution is small, the eddy current system operates in a linear manner with respect to input variations.

As explained in section 4.3.3, using the PDFs of noise and flaw signal, one can determine a threshold value which is then used for estimating the POD of the flaw. The PDFs for different flaws of varying widths and a constant depth of 0.25 mm were generated. The threshold was selected using the first criterion so that the probability of false alarm, which is independent of the flaw size, is equal to 0.05. A threshold value of 21.641938 Ohms was obtained and the PODs for the various flaws were computed. This result is plotted in Figure 5.5. The POD curve indicates that a flaw of width 0.172 mm will be detected with a probability of 0.52 whereas a larger flaw with width of 0.43 mm has a detection probability of 0.99 demonstrating the increase in probability of detection of the flaw with increasing width.

5.4.3. Effect of Multiple Sources of Variability

The second test involved the study of simultaneous effects of variations in liftoff, material conductivity and surface roughness, modeled by a multivariate normal. The mean vector and covariance matrix of the input distribution are given in Table 5.3. The measurement model was perturbed using the multivariate random normals. The dimensions of the flaw cross-section were chosen to be 0.25 mm width and 0.25 mm depth. The

Table 5.3. Parameters of the univariate normals modeling the variabilities in liftoff, material conductivity and surface roughness

Distribution	Mean	Standard deviation	Coefficient of skewness	Kurtosis
Liftoff (mm)	56.0 E-2	9.77 E-3	4.2 E-2	2.94
Material conductivity (Siemens/mm)	17.337 E +3	8.47 E+2	5.73 E-2	3.06
Surface roughness (mm)	10.0 E -5	3.0 E+2	4.5 E-2	3.0

Table 5.4. Parameters of the noise and flaw signal distributions due to the variabilities described in Table 5.3

Distribution	Mean	Standard deviation	Coefficient of skewness	Kurtosis
(<u>Liftoff variability</u>)				
No flaw signal (Ohms)	21.62	9.23 E-3	4.17 E-2	3.05
Flaw signal (Ohms)	21.6478	8.4 E-3	3.73 E-2	3.05
(<u>Material conductivity variability</u>)				
No flaw signal (Ohms)	21.6275	8.12 E-3	1.38 E-1	3.07
Flaw signal (Ohms)	21.6856	7.83 E-3	1.353 E-1	3.07
(<u>Surface roughness variability</u>)				
No flaw signal (Ohms)	21.6635	9.15 E-3	- 6.49 E-2	2.96
Flaw signal (Ohms)	21.6856	9.17 E-3	- 1.14 E-1	3.04

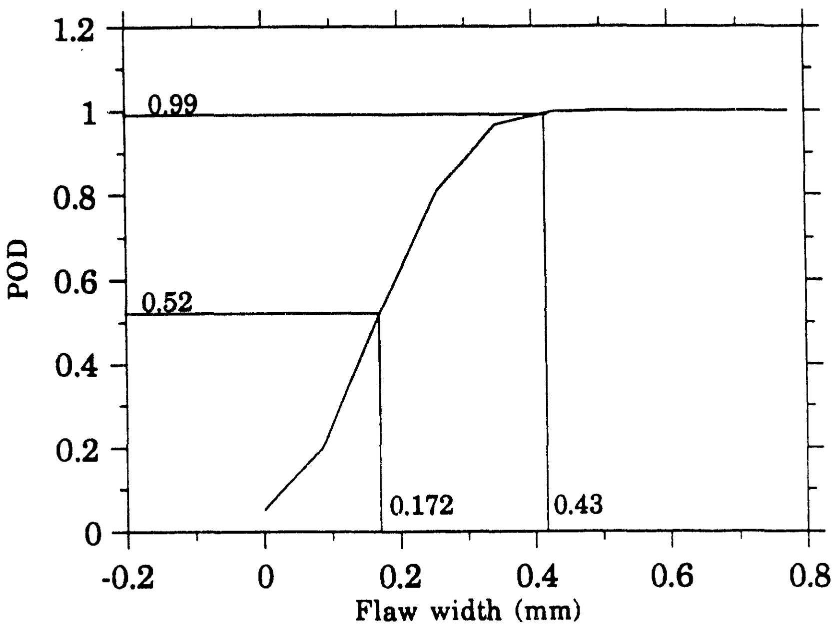

Figure 5.5: POD vs flaw width curve

corresponding conditional PDFs of the measurement variable, in the presence and absence of the flaw, were generated using model predictions. These PDFs are shown in Figure 5.6. The parameters of the model predicted signals are as summarized in Table 5.5. As expected the standard deviations for the distributions are higher relative to the earlier test with univariate perturbations.

PDFs for different flaws of varying widths and constant depth of 0.25 mm were generated and the threshold was selected by setting the PFA to 0.05 (criterion 1). A threshold value of 21.678779 Ohms was obtained. Using this

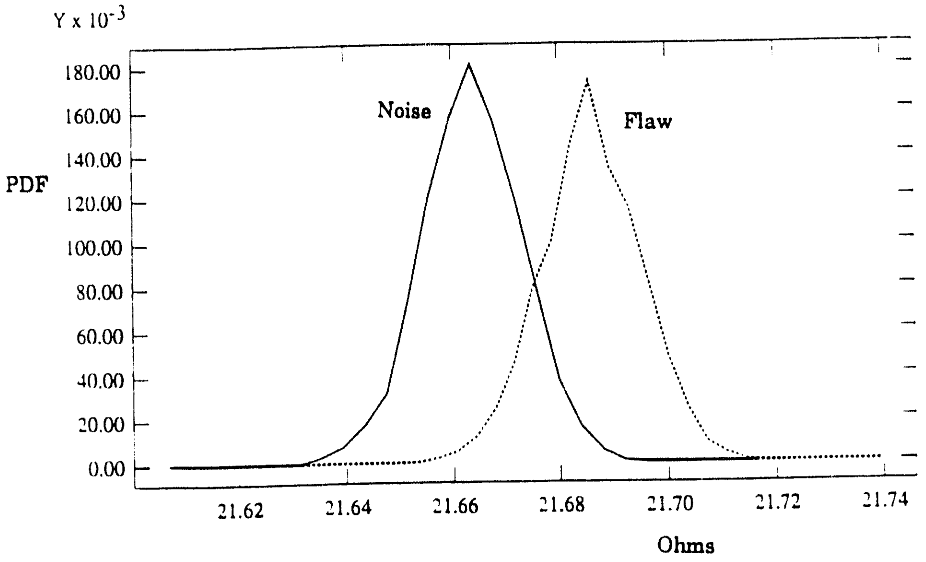

Figure 5.6: PDFs for the noise and flaw signal with the variabilities liftoff, material conductivity and roughness variabilities, modeled by a multivariate normal

threshold the PODs for the various flaws were computed. Figure 5.7 gives the plot of the POD vs flaw width for both the tests 1 and 2. The detection probabilities for test 2, where all the three variabilities are perturbing the measurement model is lower compared to the values obtained in test 1. For instance a flaw of width 0.258 mm has a POD of 0.81 in the test 1 due to the influence of liftoff and in test 2 the POD is reduced to 0.77 due to the influence of liftoff as well as material conductivity and surface roughness.

Table 5.5. Parameters of noise and flaw signal distributions with due to the variabilities described in Table 5.3 modeled by a multivariate normal

Distribution	Mean	Standard deviation	Coefficient of skewness	Kurtosis
Noflaw signal (Ohms)	21.6637	9.25 E-3	- 5.53 E-2	2.94
Flaw signal (Ohms)	21.6857	9.23 E-3	-1.08 E-1	3.03

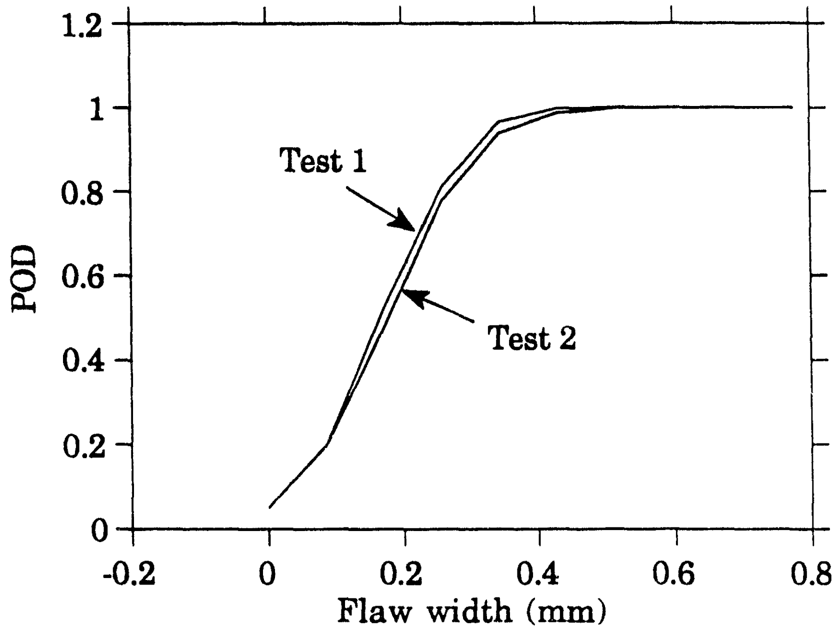

Figure 5.7: POD curves showing the influence of the various variabilities acting on the test system

5.4.4. Effect of Threshold

The third experiment involved the demonstration of the effect of different choice of thresholds on the probability of detection of defects. The importance of such a study has been explained earlier in chapter 4. The results obtained by the selection of different thresholds are presented here.

In general, the detection probabilities of small flaws is very sensitive to the value of threshold chosen. Figure 5.8 shows the PDFs of the eddy current

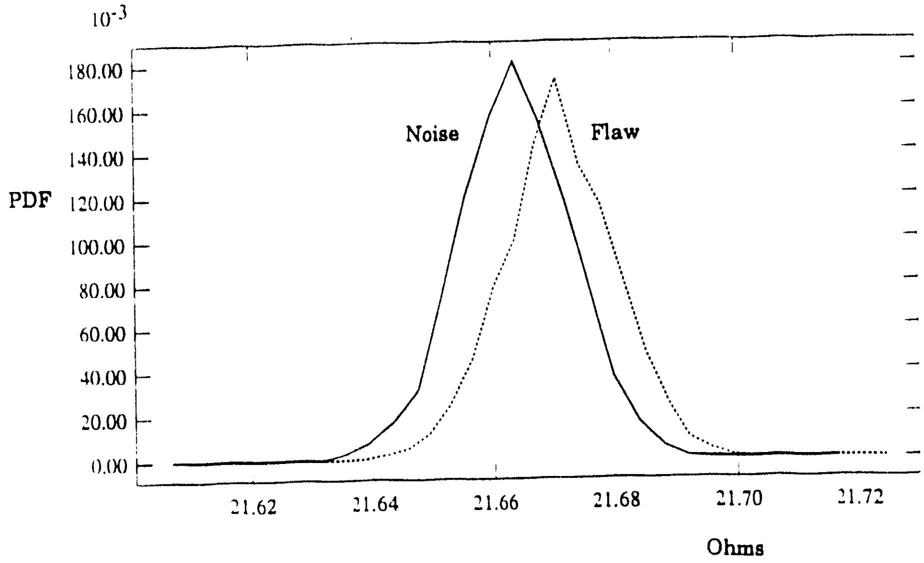

Figure 5.8. PDFs in the presence and absence of a flaw

signal in the presence and absence of a small axisymmetric flaw of dimensions 0.1 mm width and 0.25 mm depth. Once a threshold T is selected, signals whose magnitude exceeds T are interpreted as flaw signals and signals with magnitude below T are interpreted as noise.

As seen in Figure 5.8 a low value of the threshold would result in a high probability of detecting the flaw. This would also result in a high false alarm rate. On the contrary a high value of threshold would result in a low PFA but also a smaller probability of detection of the flaw and a high false acceptance rate. The POD and PFA value pairs for decreasing values of the thresholds were computed and are plotted in the ROC curve in Figure 5.9. The ROC curve

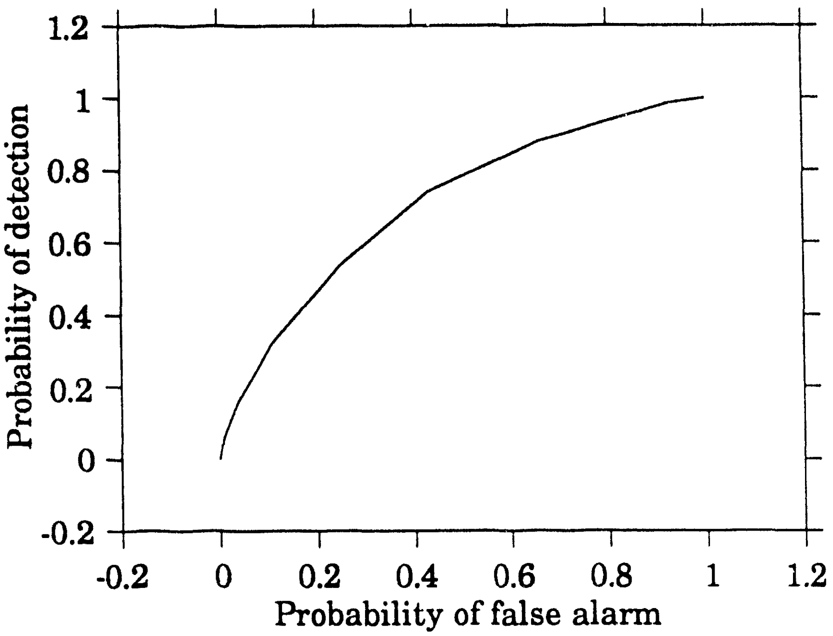

Figure 5.9: Relative Operating Characteristics of the system

enables one to determine what the POD of a flaw would be if the threshold was selected so as to fix the PFA to an allowable constant value.

The corresponding PFA vs POFA curve is plotted in Figure 5.10, where it is seen that thresholds for low value of PFA result in a high POFA and vice versa. From economic and safety considerations low PFA and POFA rates are desired and hence the selection of an optimum value of the threshold plays a very important role. A number of studies were conducted in order to demonstrate the effects of the choice of thresholds using different criteria, discussed in chapter 4. Nine flaws of different dimensions were machined on a

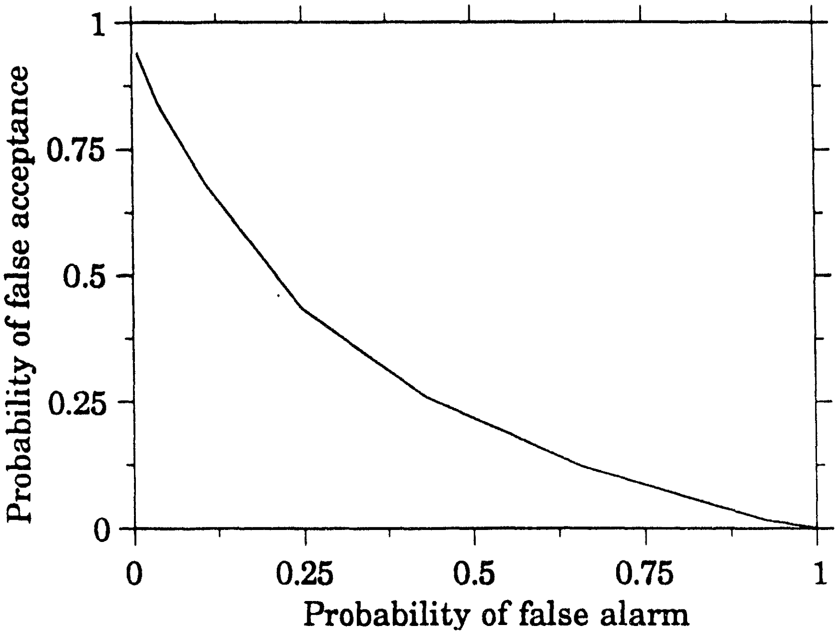

Figure 5.10. PFA vs POFA at different values of threshold

curved aluminum plate. The thickness of the aluminum plate is 6 mm and the location of the flaws with respect to the plate are shown in Figure 5.11. The dimensions of the 9 axisymmetric flaws are as summarized in Table 5.7. The measurement variabilities liftoff, material conductivity and surface roughness were modeled by a multivariate normal. The measurement model was perturbed using the multivariate random normals and the PDFs of the nine flaws generated using the model predictions. Once the PDFs were generated a threshold was selected using the three criteria as explained below.

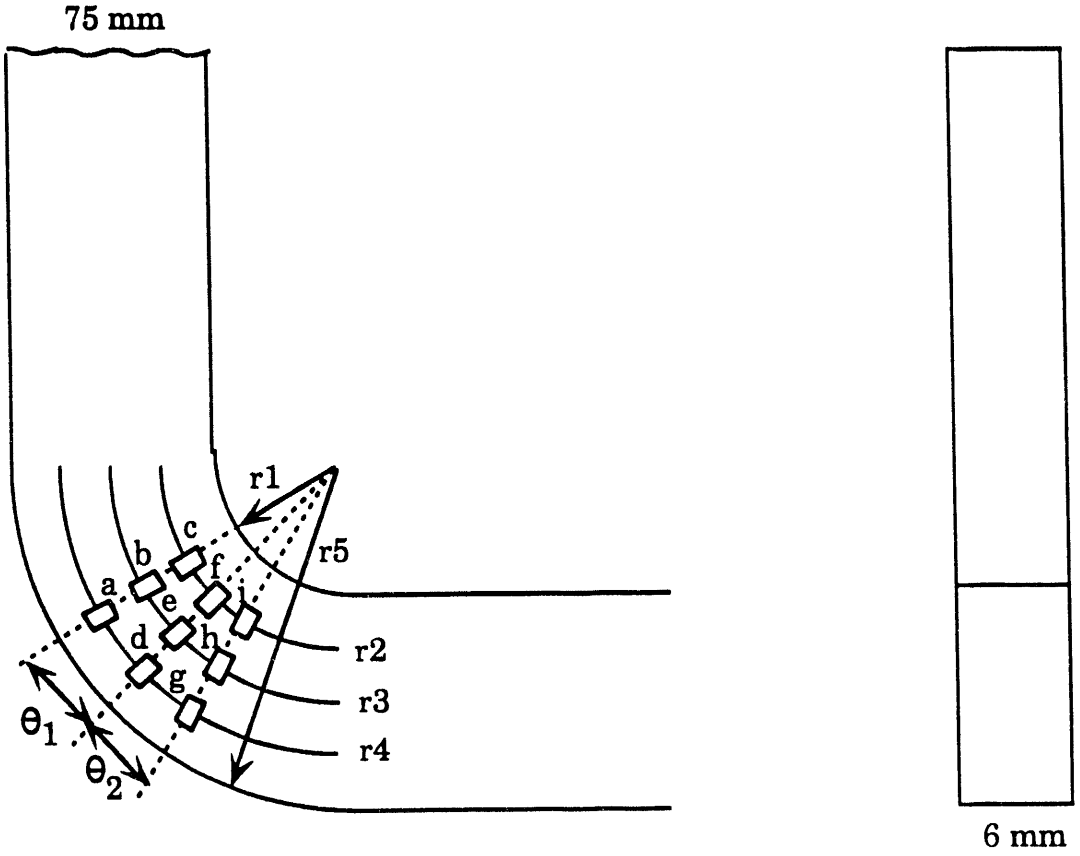

r1 = 30 mm; r2 = 55 mm; r3 = 65 mm; r4 = 75 mm; r5 = 105mm.

$\theta_1 = 35°$ $\theta_2 = 35°$

Figure 5.11: Nine different flaws machined on a curved aluminum plate

Table 5.7. Dimensions of the nine different flaws

Flaw	Width (mm)	Depth (mm)
a	0.125	0.50
b	0.125	1.00
c	0.125	1.5
d	0.25	0.25
e	0.25	1.00
f	0.25	2.5
g	0.25	1.25
h	0.50	1.25
i	1.25	1.25

1. Criterion 1: A threshold value, T_1, of 21.6787 Ohms was obtained by setting the value of PFA to 0.05. The corresponding POD and PFA for the nine flaws are as shown in the Table 5.8.

2. Criterion 2: The flaw 'e' was selected to be the critical flaw and the threshold, T_2, equal to 21.716 Ohms was obtained such that the POD of the flaw e is 0.95. The corresponding POD and PFA values for the nine flaws computed using this threshold are as summarized in Table 5.9.

Table 5.8. POD and PFA for the 9 different flaws with threshold, T_1, selected using criterion 1 equal to 21.6787 Ohms

Defect	POD	PFA
a	0.58	0.05
b	0.58	0.05
c	0.58	0.05
d	1.0	0.05
e	1.0	0.05
f	1.0	0.05
g	1.0	0.05
h	1.0	0.05
i	1.0	0.05

Table 5.9. POD and PFA for the 9 different flaws with threshold, T_2, selected using criterion 2 equal to 21.716 Ohms

Defect	POD	PFA
a	0.04	0.0
b	0.04	0.0
c	0.04	0.0
d	0.871	0.0
e	0.95	0.0
f	0.9528	0.0
g	0.9510	0.0
h	1.0	0.0
i	1.0	0.0

3. Criterion 3: For each of the 9 flaws, the threshold, T_3, was selected by minimizing the weighted sum of the overall signal classification errors (false alarm and false acceptance rates). The corresponding probability of detection and probability of false alarm were computed using this threshold. The thresholds and the corresponding POD and PFA values for each of the 9 flaws are as shown in Table 5.10.

Comparing the results in Table 5.8 with that in Table 5.9, it is seen that since the threshold value , T2, is greater than that in the former case, T_1, the corresponding POD and PFA values are lower. Table 5.10 enables one to determine the probability of detection and probability of false alarm of a flaw would be when the signal classification is made such that the weighted sum of the classification errors is a minimum. This technique is particularly useful technique is particularly useful when a priori knowledge of the probability of finding a flaw in a part is available. The threshold can be selected such that the weighted sum of the signal classification error for the critical flaw size is a minimum. Using this threshold value the probability of detection and probability of false alarm of flaws of other dimensions can be determined.

Table 5.10. The threshold, POD and PFA values for the 9 flaws

Defect	Threshold (Ohms)	POD	PFA
a	21.6777	0.7388	0.19
b	21.6777	0.7388	0.19
c	21.6777	0.7388	0.19
d	21.6797	0.9066	0.04
e	21.6819	0.9776	0.02
f	21.6820	0.9826	0.02
g	21.6320	0.9790	0.02
h	21.6947	1.0	0.0
i	21.6947	1.0	0.0

CHAPTER 6. CONCLUSIONS AND FUTURE WORK

6.1. Summary

This thesis investigates the feasibility of using a numerical model in a probabilistic framework for estimating the probability of detecting a flaw in the presence of measurement variabilities. Numerical models have been extensively used to characterize physical processes underlying NDE phenomena. A numerical finite element model simulating eddy current NDE phenomena, explained in detail in chapter 3, is employed as a tool for predicting the probe response for a given geometry. However these models are deterministic in nature and do not take into account the variability associated with the inspection process carried out in the field. This results in a considerable difference between the nominal value of the transducer response predicted by the model and the actual measurement.

The probability of detection model consists of modeling the different sources of measurement variabilities by univariate or multivariate Gaussian distributions. Samples from the distribution are used to perturb the finite element measurement model. Using a Monte Carlo simulation procedure the numerical model predicts the univariate conditional probability density functions of the measurement variable for flaws of different dimensions. The conditional distributions in the presence and absence of a flaw can be treated as a weighted mixture of distributions and used for estimating the probability of detection and probability of false alarm for defects of various dimensions.

Results demonstrating the feasibility of the model based approach for estimating the detection probability of defects are presented.

6.2. Future Work

The limitation of the two dimensional probability of detection model, however, is the inability to incorporate all the variabilities that occur in an NDT system. The 2D POD model, for eddy current NDT, incorporates variabilities such as liftoff, material properties and surface roughness. However the variabilities that occur in a practical test setup include probe canting angle and scan related factors which can only be modeled using a full 3D POD model. The steps involved in the development of the 3D POD model and the challenges associated with it are explained here.

The major difficulties in 3D POD modeling are

1. Generation of accurate 3D meshes
2. Memory resources and
2. Simulation time.

6.2.1. Application of CAD for generation of accurate 3D meshes

A fundamental problem in three dimensional finite element models is the generation of 3D meshes for complex geometries. Commercial finite element packages allow the creation of 3D meshes with relative ease, however these packages do not offer flexibility to the user for further adaptation.

In order to overcome the problems associated with the generation of 3D geometries and their meshes the CAD package, I-DEAS, released by the Structural Dynamics Research Corporation (SDRC), is being considered. The two stages involved in the use of the CAD package for 3D finite element mesh creation are solid modeling and mesh generation which are explained in more detail next.

Solid Modeling In the first step the information about geometrical parameters are input to the CAD package. Figure 6.1 shows the solid model of a curved aluminum plate with 9 flaws of different dimensions machined on it. Figure 6.2 is a solid model of a lap joint with two rows of rivets on the plates.

The solid modeling starts with a 2D sketch of the geometry wherein tools for drawing the arcs, lines, splines etc are used to input the 2D sketch of the geometry. Using the object modeling, the 2D sketch can be extruded in the third dimension in order to arrive at the full 3D geometry. This CAD package is especially useful for modeling complex geometries as it contains many useful features such as merging two different objects into one, cutting one object by another and modifying parts of an object. Once the solid model is created the next stage would involve discretization of the object with a suitable mesh.

Mesh Creation The CAD package contains several useful features that enables the generation of a 3D finite element mesh with relative ease. Some of these features include linear or nonlinear elements and triangular, quadrilateral or cubic wedge shaped elements. Utilities for checking the quality of the mesh for free edges, coincident elements, warping and distortion

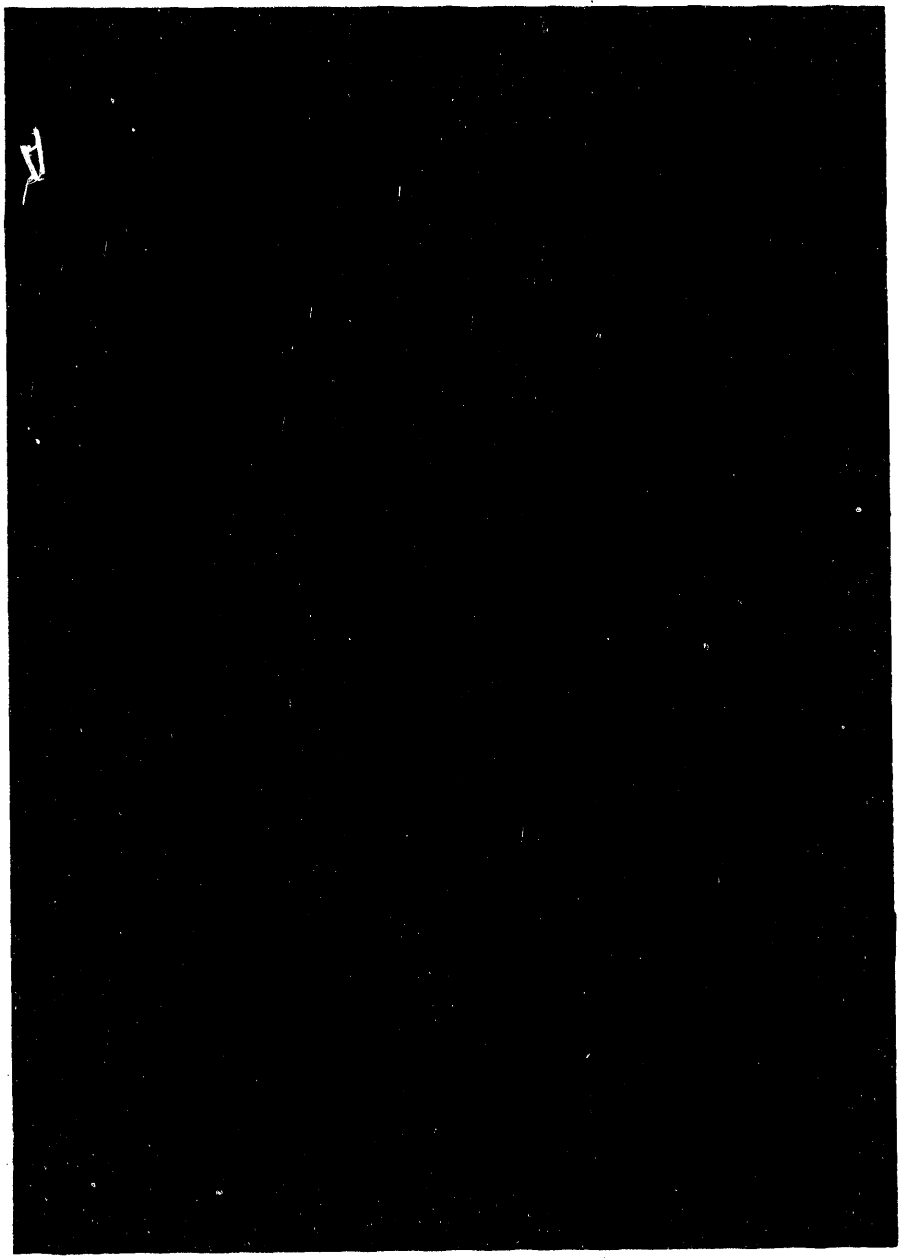

Figure 6.1: Solid model of a curved aluminum plate with flaws machined onto it

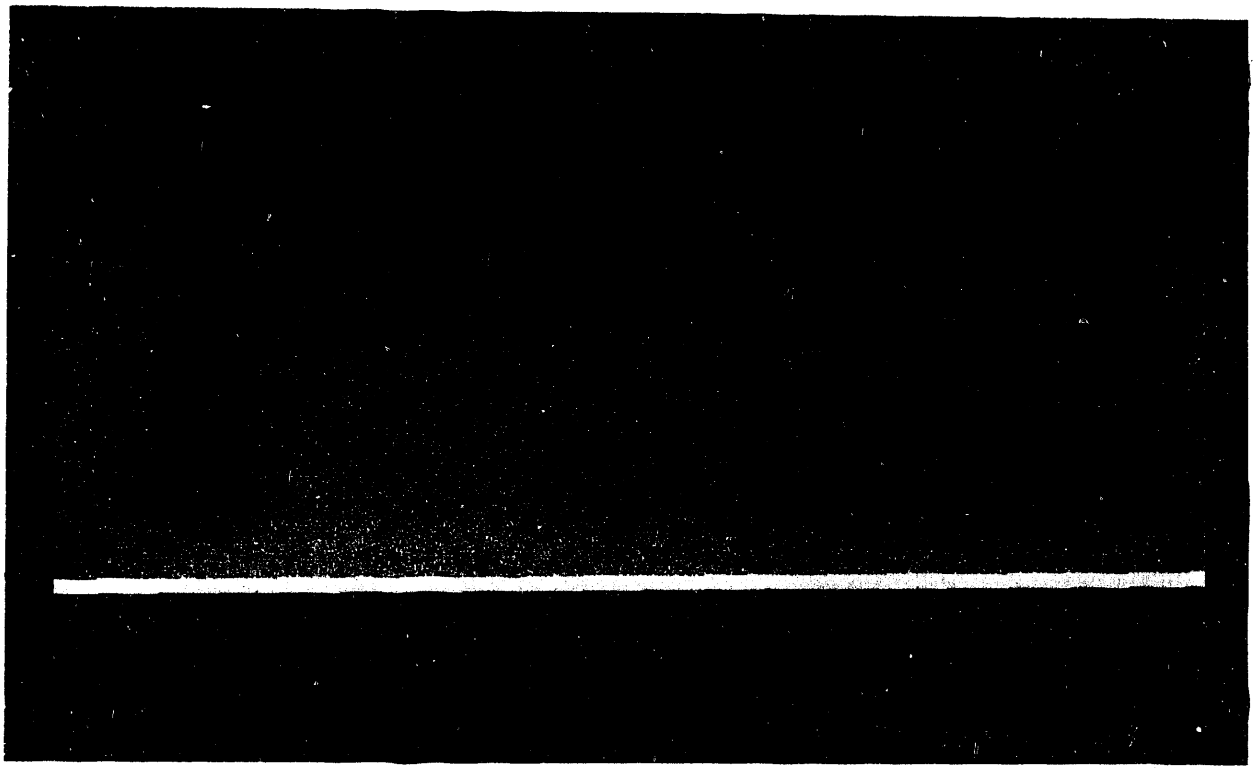

Figure 6.2: Solid model of a lap joint with two rows of rivets

are also available. The utilities provide value parameters such as distortion value, warping value and stretch value for each element. Finally options for arriving at an optimum numbering sequence for the elements, in order to reduce the bandwidth, can be used for mesh optimization. This in turn results in a large reduction in solution time and the computer resources such as memory and disk space.

6.2.2. Simulation Time

One of the most important factors that have to be considered for 3D POD modeling is the simulation time. For instance a single simulation of the 2D POD model takes 2 minutes of CPU time on a DEC 5000 machine. The model therefore generates a signal distribution containing 2500 samples in roughly 2500 x 2 minutes = 3.4 days. However a single simulation process using a 3D finite element model requires 8 hours CPU time and it would therefore take about 2500 x 8 hours = 2.3 years to generate a reasonable distribution. The estimation of the POD of flaws would involve the generation of many such distributions and hence the use of the 3D POD model is not economically feasible.

However the advances in the computer technology have resulted in the availability of large and fast computers, particularly the new super computer like the Cray YMP and the massively parallel machines like the MasPar. One area of research in progress currently is the adaptation of the 3D measurement model, on these parallel and vector machines.

Another technique that can be used for the reduction of the number of simulations required to generate the POD curve is a modified Monte-Carlo simulation technique known as the importance sampling technique, which is described briefly next.

6.2.3. Importance Sampling Technique [43]

The estimation of the parameters such as POD and PFA for a given flaw, basically involves the integrations of the tail regions of distributions. However the estimation of these integrations with a reasonable accuracy requires a large number of samples in the distribution and hence a large simulation time. For instance from equation (4.5) the probability of false alarm is expressed as

$$PFA = \int_T^\infty f_Y(y)\,dy \qquad (6.1)$$

where $f_Y(y)$ is the noise PDF and T the threshold value selected. The number of samples, N, required to estimate this integration using the Monte-Carlo simulation technique is given by

$$N > \frac{1}{\varepsilon^2 (PFA)} \qquad (6.2)$$

where ε is the normalized error in the estimated PFA and is given by

$$\varepsilon = \frac{\text{Standard deviation of the estimated PFA}}{\text{PFA}} \qquad (6.3)$$

From equation (6.2), an ε of 0.1 requires a sample size greater than or equal to $\frac{100}{\text{PFA}}$. A PFA value of 0.05 requires a sample size, N, of about 2000.

Importance sampling technique [43] consists on transforming the density function $f_Y(y)$ to a PDF $f_Y^*(y)$ such that the probability of a sample occurring in the tail region in the new distribution is higher. This is illustrated in Figure 6.3. The probability of false alarm given by equation (6.1),

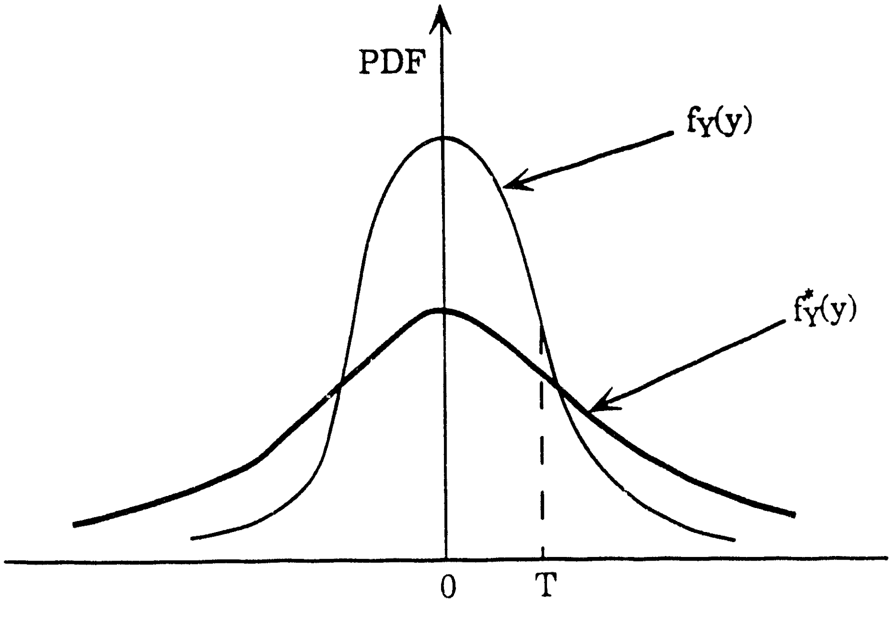

Figure 6.3: Representation of the warping of the PDF involved in the importance sampling technique

can be rewritten in the form

$$PFA = \int_{-\infty}^{\infty} h(y)\, f_Y(y)\, dy \tag{6.4}$$

where $h(y) = 1$ if $y \geq T$

$= 0$ if $y < T$.

Equation (6.4) can be further rewritten as

$$PFA = \int_{-\infty}^{\infty} h(y) \frac{f_Y(y)}{f_Y^*(y)} f_Y^*(y)\, dy \tag{6.5}$$

$$= \int_{-\infty}^{\infty} h^*(y) f_Y^*(y)\, dy \tag{6.6}$$

The ratio $\frac{f_Y^*(y)}{f_Y(y)}$ is called the bias of the random variable Y at $Y = y$ in the distribution. Equation 6.6 is nothing but the mean value of $h^*(y)$ given by

$$PFA = \frac{1}{N} \sum_{i=1}^{N} h^*(y_i) \tag{6.7}$$

where y_i's are the values sampled on the new distribution $f_Y^*(y)$. The tail probability in the new distribution is obtained with significantly reduced number of simulations. The PFA estimated with the new distribution is then transformed back to the corresponding value under the true distribution.

6.3. Conclusions

The results presented indicate the feasibility of using a numerical finite element model in a probabilistic framework. The stochastic model in turn is used to determine the probability of detecting a given defect. The various concepts involved in the estimation of the probability of detection of a flaw have been presented.

One of the deficiencies of the model based approach is the lack of exact knowledge of the statistical properties of the measurement noise and other sources of variability. All results obtained in this thesis are based on the assumption of a Gaussian distribution for the various factors such as lift off, surface roughness and material properties. It is therefore essential to use experimental POD models for validation. However the model based approach has several significant advantages:

1. Model based approaches complement experimental POD models
2. Cost of generating POD curves are very low
3. Complex defect shapes can be handled easily and
4. The results are operator independent.

BIBLIOGRAPHY

[1] Halmshaw, R. *Non-destructive Testing*. Edward Arnold (Publishers) Ltd., London, 1987.

[2] Libby, H. L. *Introduction to Electromagnetic Nondestructive Test Method.* Robert E. Krieger publishing company, New York, 1979.

[3] Satish, S. R. "Parametric Signal Processing for Eddy Current NDT." Ph. D. Dissertation, Colorado State University, Ft. Collins, 1983.

[4] Udpa, L. "Imaging of Electromagnetic NDT Phenomena." Ph. D. Dissertation, Colorado State University, Ft. Collins, 1985.

[5] Zienkiewicz, O. C. *The Finite Element Method in Engineering Science*, McGraw Hill, London, 1971.

[6] Wilson, E. L. and Nickel, R. E. *Application of the Finite Element Method to Heat Conduction Analysis*, Nuclear Engineering and Design, Vol. 4, 1966, p 276-286.

[7] Silvester, P. and Chari, M. V. "Finite Element Solutions of Saturable Magnetic Field Problems." In *IEEE Transactions on Power Apparatus and Systems*, Vol. PAS-89, No. 7, September 1970, p 1642-1648.

[8] Chari, M. V. and Silvester, P. "Analysis of Turbo - Alternator Magnetic Fields by Finite Elements." *International Bibliography, Information and Documentation*, Vol. PAS-90, No. 2, March 1971, p 168-175.

[9] Demerdash, N. A. et al., "Simulation for design Purposes of Magnetic Fields in Turbogenerators with Symmetrical and Asymmetrical Rotors-Part I - Model Development and Solution Technique." *International Bibliography, Information and Documentation*, Vol. PAS-91, 1972, p 501-510.

[10] Chari, M. V. "Finite Element Solution of the Eddy Current Problem in Magnetic Structures." *IEEE Transactions on Power Apparatus and Systems*, Vol. PAS-93, No. 1, Jan. 1974, p 62-72.

[11] Anderson, O. W. "Transformers Leakage Flux Program Based on the Finite Element Method." *International Bibliography, Information and Documentation*, Vol. PAS-92, No. 2, March 1973, p 38-45.

[12] Brauer, J. R. "Finite Element Analysis of Electromagnetic Induction in Transformers." *Presented at the IEEE Winter Power Meeting*, New York, Jan. 1977.

[13] Hwang, J. H. and Lord, W. "Finite Element Modeling of Magnetic Field/Defect Interactions." *In ASMT Journal of Testing and Evaluation*, Vol. 3, No. 1, Jan. 1975, p 21-25.

[14] Hwang, J. H. and Lord, W. "Magnetic Leakage Field Signatures of Material Discontinuities." *In Proceedings of the Tenth Symposium on NDE*, San Antonio, Texas, April 1975.

[15] Yen, W. C. "Finite Element Characterization of Residual Leakage Fields." M. S. Thesis, Colorado State University, Ft. Collins, 1978.

[16] Udpa, S. S. and Lord, W. "Finite Element Modeling of Residual Magnetic Phenomenon." *Presented at the International Magnetics Conference*, Boston, April 1980.

[17] Lord, W. and Palanisamy, R. "Magnetic Probe Inspection of steam Generator Tubing." *Materials Evaluation*, Vol. 38, No. 5, May 1980, p 478-485

[18] Palanisamy, R. and Lord, W. "Finite Element Analysis of Eddy Current Phenomena." *International Bibliography, Information and Documentation*, Vol. 38, No. 10, October 1980, p 901-913.

[19] Palanisamy, R. and Lord, W. "Finite Element Analysis of Axisymmetric Geometries in Quantitative NDE." *In Review of Progress in Quantitative NDE*, San Diego, July 1979.

[20] Ida, N. "Three Dimensional Finite Element Modeling of Electromagnetic NDT phenomena." Ph. D. Dissertation, Colorado State University, Ft. Collins, 1983.

[21] Ida, N. and Lord, W. "3-D Finite Element Prediction of Magnetostatic Leakage Fields." *In IEEE Transactions on Magnetics*, September 1983, p 2260-2265.

[22] Pars, L. A. *An Introduction to Calculus of Variations.* Heineman, London, 1962.

[23] Ortega, J. M. and Rheinboldt, W. C. *Iterative Solution of Nonlinear Equations in Several Variables.* Academic Press, New York, 1970.

[24] Issacson, E. and Keller, H. B. *Analysis of Numerical Methods*, John Wiley and Sons, New York, 1966.

[25] Zienkiewicz, O. C. *The Finite Element Method*, McGraw Hill Book Company, New York, 1977.

[26] Norrie, D. H. and Vries, G. *The Finite Element Method*, Academic Press, New York and London, 1973.

[27] Dodd, C. V. "Solutions to Electromagnetic Induction Problems.", Ph. D. Dissertation, University of Tennessee, 1967.

[28] Palanisamy, R. "Finite Element Modeling of Eddy current Nondestructive Testing Phenomena." Ph. D. Dissertation, Colorado State University, Ft. Collins, 1980.

[29] Ida N. "Alternative Approaches to the Numerical Calculation of Impedance", *NDT International.* Vol. 21 No. 1, Feb 1988, p 27-35.

[30] Hoole, Ratnajeevana, *Computer Aided Analysis and Design of Electromagnetic Devices*, Elsevier Science Publishing Co. Inc., New York 1989.

[31] Richardson, J. M. and Buckley, M. J. "Overview of Probabilistic Failure Prediction and Accept-Reject Decisions" *In Review of Progress in Quantitative NDE,* Vol. 1, edited by D. O. Thomson and D. E. Chementi, Plenum Press, New York, July 1982, p 43-58.

[32] Lewis, W. H., Sproat, W. H., Dodd, B. D. and Hamilton, J. M. *Reliability of Nondestructive Inspections - Final Report*, SA-ALC/MME 76-6-38-1, San Antonio Air Logistics Center, Kelly Air Force Base, Dec 1978.

[33] Berens, A. P. and Hovey, P. W. *Evaluation of NDE Reliability Characterization*, AFWAL-TR-81-4160, Vol 1, Air Force Wright-Aeronautical Laboratories, Wright-Patterson Air Force Base, Dayton, OH, Dec 1981.

[34] Berens, A. P. and Hovey, P. W. "Statistical Methods for Estimating Crack Detection Probabilities." In Probabilistic Fracture Mechanics and Fatigue Methods: Applications for Structural Design and Maintenance, STP 798, Bloom, J. M. and Ekvall, J. C. Ed., *American Society for Testing and Materials,* 1983, p 79-94.

[35] Allison, D. E. et al. *Cost/Risk Analysis for Disk Retirement - Volume I.* AFWA-TR-83-4089, Air Force Wright Aeronautical laboratories, Wright Patterson Air Force Base, Dayton, OH, Feb 1984.

[36] Berens, A. P. and Hovey, P. W. *Flaw Detection Reliability Criteria Volume I- Methods and Results*, AFWAL-TR-84-4022, Air Force Wright Aeronautical Laboratories, Wright Patterson Air Force Base, Dayton, OH, April 1984.

[37] Alan P. Berens, “NDE Reliability Data Analysis”, In *Metals Handbook*, Vol. 11, 9th Edition, Nondestructive Evaluation and Quality Control.

[38] Rajesh, S. N., Udpa, L., Udpa, S. S. and Nakagawa, N. "Probability of Detection Models for Eddy Current NDE Methods" *In Review of Progress in Quantitative NDE,* Vol. 11A, edited by D. O. Thomson and D. E. Chementi, Plenum Press, New York, July 1991, p 265-275.

[39] Rajesh, S. N., Udpa, L. and Udpa, S. S. "Numerical Model Based Approach for Estimating Probability of Detection in NDE Applications", *IEEE Conference of Electromagnetic Field Computation*, June 1992, p 385-395.

[40] Rajesh, S. N., Udpa, L. and Udpa, S. S. "Estimation of Eddy Current Probability of Detection Using Finite Element Method", *In Review of Progress in Quantitative NDE,* edited by D. O. Thomson and D. E. Chementi, Plenum Press, New York, July 1992, p 816-823.

[41] Gonzalez Rafael C. and Wintz, Paul. *Digital Image Processing*. Second Edition, Addison Publishing Company, Inc, Massachusetts, Nov 1987.

[42] Gupta, C. B. *An Introduction to Statistical Methods*. M/S Ramprasad and Sons, Agra, India, 1957.

[43] Shanmugam, K. S. and Balaban, P. "A Modified Monte-Carlo Simulation Technique for the Evaluation of Error Rate in Digital Communication." In *IEEE Transactions on Communications*, Vol. Com- 28, No. 11, Nov 1980, p 1916-1924.

[44] Edwin, H. Chen. "A Random Normal Number Generator for 32-Bit-Word Computers. "*Journal of the American Statistical Association*. June 1971, Vol 66, No 334, Theory and Methods Section, p 400-403.

[45] Ross, Sheldon. M. *Introduction to Probability Models*, Fourth Edition, Academic Press, Inc., San Diego, 1985.

APPENDIX

Random Normal Number Generator [44]

Box Muller Method Two independent random normal deviates, X1 and X2, of zero mean and unit variance can be produced from two independent uniform deviates, U1 and U2, by the transformation suggested by Box and Muller given by the equations

$$X_1 = (-2 \ln U_1)^{\frac{1}{2}} \cos(2\pi U_2) \tag{1}$$

$$X_2 = (-2 \ln U_1)^{\frac{1}{2}} \sin(2\pi U_2). \tag{2}$$

Normal random numbers of a different mean and variance can be obtained by suitable linear transformation [45] of the Xi's.

END

DATE
FILMED
3/14/94